The Primordial Inflation Explorer (PIXIE): Mission Design and Science Goals

Alan Kogut, Nabila Aghanim, Jens Chluba, Dave Chuss, Jacques Delabrouille, Cora Dvorkin, Dale Fixsen, Brandon Hensley, Colin Hill, Bruno Maffei, et al.

The Primordial Inflation Explorer (PIXIE): mission design and science goals

Journal of Cosmology and Astroparticle Physics
An IOP and SISSA journal

Received: *June 3, 2024*
Revised: *December 13, 2024*
Accepted: *March 6, 2025*
Published: *April 8, 2025*

The Primordial Inflation Explorer (PIXIE): mission design and science goals

Alan Kogut,[a,*] **Nabila Aghanim**,[b] **Jens Chluba**,[c] **David T. Chuss**,[d] **Jacques Delabrouille**,[e] **Cora Dvorkin**,[f] **Dale Fixsen**,[a,g] **Shamik Ghosh**,[h,e] **Brandon S. Hensley**,[i] **J. Colin Hill**,[j,k] **Bruno Maffei**,[l] **Anthony R. Pullen**,[m,k] **Aditya Rotti**,[c] **Alina Sabyr**,[n] **Eric R. Switzer**,[a] **Leander Thiele**,[o,p] **Edward J. Wollack**[a] **and Ioana Zelko**[q]

[a] *NASA Goddard Space Flight Center, 8800 Greenbelt Road, Greenbelt, MD 20771, U.S.A.*
[b] *Université Paris-Saclay, CNRS, Institut d'Astrophysique Spatiale, Bâtiment 121, 91405 Orsay, France*
[c] *Jodrell Bank Centre for Astrophysics, Department of Physics and Astronomy, The University of Manchester, Manchester M13 9PL, U.K.*
[d] *Department of Physics, Villanova University, 800 Lancaster Avenue, Villanova, PA 19085, U.S.A.*
[e] *CNRS-UCB International Research Laboratory, Centre Pierre Binétruy, IRL 2007, CPB-IN2P3, Berkeley, CA 94720, U.S.A.*
[f] *Department of Physics, Harvard University, 17 Oxford Street, Cambridge, MA 02138, U.S.A.*
[g] *Department of Astronomy, University of Maryland, College Park MD 20740 U.S.A.*
[h] *Lawrence Berkeley National Laboratory, 1 Cyclotron Road, Berkeley, CA 94720, U.S.A.*
[i] *Jet Propulsion Laboratory, California Institute of Technology, 4800 Oak Grove Drive, Pasadena, CA 91109, U.S.A.*
[j] *Department of Physics, Columbia University, New York, NY 10027, U.S.A.*
[k] *Center for Computational Astrophysics, Flatiron Institute, New York, NY 10010, U.S.A.*
[l] *Institut d'Astrophysique Spatiale, CNRS-Université Paris-Saclay, Orsay, 91405, France*

[*] Corresponding author.

https://doi.org/10.1088/1475-7516/2025/04/020

JCAP04(2025)020

[m] *Center for Cosmology and Particle Physics, Department of Physics, New York University, 726 Broadway, New York, NY, 10003, U.S.A.*

[n] *Department of Astronomy, Columbia University, New York, NY 10027, U.S.A.*

[o] *Kavli Institute for the Physics and Mathematics of the Universe, UTIAS, The University of Tokyo, Kashiwa, Chiba 277-8583, Japan*

[p] *Center for Data-Driven Discovery (CD3), Kavli IPMU (WPI), UTIAS, The University of Tokyo, Kashiwa, Chiba 277-8583, Japan*

[q] *Canadian Institute for Theoretical Astrophysics, University of Toronto, 60 St. George Street, Toronto, ON M5S 3H8, Canada*

E-mail: alan.j.kogut@nasa.gov, nabila.aghanim@universite-paris-saclay.fr, jens.chluba@manchester.ac.uk, david.chuss@villanova.edu, jacques.delabrouille@gmail.com, cdvorkin@g.harvard.edu, Dale.J.Fixsen@nasa.gov, shamik@lbl.gov, brandon.s.hensley@jpl.nasa.gov, jch2200@columbia.edu, bruno.maffei@u-psud.fr, anthony.pullen@nyu.edu, adityarotti@gmail.com, a.sabyr@columbia.edu, eric.r.switzer@nasa.gov, leander.thiele@ipmu.jp, Edward.J.Wollack@nasa.gov, ioana.zelko@gmail.com

Abstract: The Primordial Inflation Explorer (PIXIE) is an Explorer-class mission concept to measure the energy spectrum and linear polarization of the cosmic microwave background (CMB). A single cryogenic Fourier transform spectrometer compares the sky to an external blackbody calibration target, measuring the Stokes I, Q, U parameters to levels $\sim$200 Jy/sr in each 2.65° diameter beam over the full sky, in each of 300 frequency channels from 28 GHz to 6 THz. With sensitivity over 1000 times greater than COBE/FIRAS, PIXIE opens a broad discovery space for the origin, contents, and evolution of the universe. Measurements of small distortions from a CMB blackbody spectrum provide a robust determination of the mean electron pressure and temperature in the universe while constraining processes including dissipation of primordial density perturbations, black holes, and the decay or annihilation of dark matter. Full-sky maps of linear polarization measure the optical depth to reionization at nearly the cosmic variance limit and constrain models of primordial inflation. Spectra with sub-percent absolute calibration spanning microwave to far-IR wavelengths provide a legacy data set for analyses including line intensity mapping of extragalactic emission and the cosmic infrared background amplitude and anisotropy. We describe the PIXIE instrument sensitivity, foreground subtraction, and anticipated science return from both the baseline 2-year mission and a potential extended mission.

Keywords: CMBR experiments, CMBR polarisation, cosmological parameters from CMBR, Sunyaev-Zeldovich effect

ArXiv ePrint: 2405.20403

JCAP04(2025)020

Contents

JCAP04(2025)020

1 Introduction

The cosmic microwave background (CMB) records information across the history of the universe. Its nearly-isotropic blackbody spectrum provides compelling evidence for a primordial origin within a hot, dense system in close thermal equilibrium. The subsequent expansion and evolution to the presently observed structures perturbs the CMB, with cosmological information encoded within its frequency spectrum, spatial anisotropy, and polarization.

Observations of cosmological radiation backgrounds have played a key role in our understanding of the universe. Measurements of the CMB frequency spectrum [1–26] are consistent with a single blackbody over a range of 3 decades in frequency and 4 decades in intensity (figure 1). Data from the COBE/FIRAS spectrometer determine the monopole temperature $T_0 = 2.72548 \pm 0.00057\,\mathrm{K}$ [27]. The FIRAS limits on deviations from a blackbody spectrum (spectral distortions) at levels $\Delta I/I < 5 \times 10^{-5}$ [25] support the thermal hot big bang model while ruling out alternatives such as steady state models [28]. Measurements of CMB anisotropies in temperature and polarization have provided insight into the contents of the universe and their evolution from primordial density perturbations to matter clustering, reionization, and the growth of large scale structure, consistent with a single 7-parameter cosmological model (ΛCDM, [29, 30]).

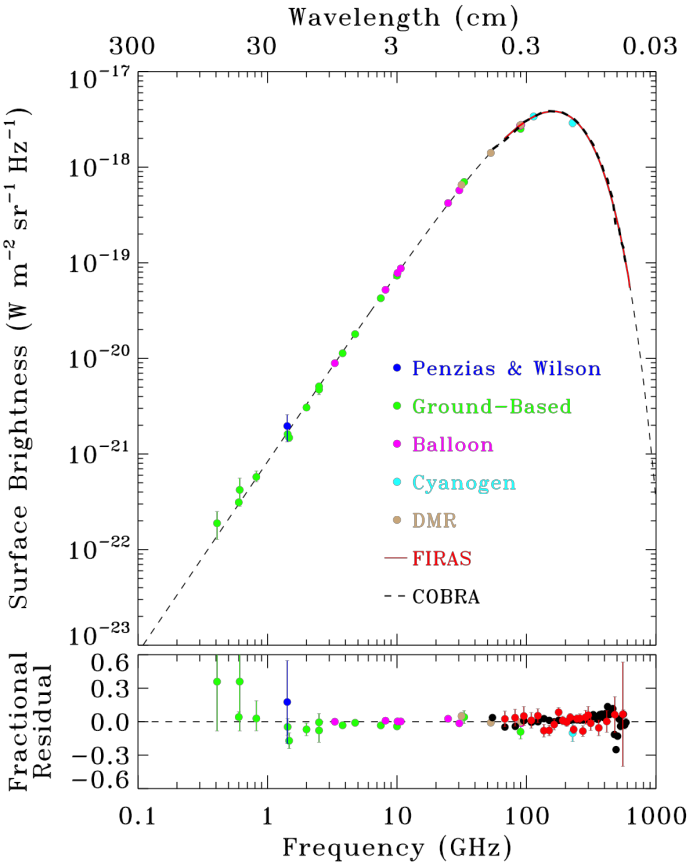

Figure 1. Measurements of the CMB spectrum are consistent with a single blackbody (dashed line). The top panel shows selected precise measurements while the bottom panel shows fractional residuals about the best-fit blackbody. The FIRAS residuals have been increased 1000× for visibility.

Despite its success, this model is manifestly incomplete. It requires both dark energy and dark matter, neither of which exist within the Standard Model of particle physics. The observed flat geometry and nearly scale-invariant distribution of density perturbations hint at an origin in a period of exponential expansion called inflation, but direct evidence for inflation is missing. The process by which baryons collapse to form galaxies is not fully understood, nor why star formation has declined by a factor of 10 over the past 10 billion years.

Precise measurements of the CMB introduce new opportunities to study the early universe and understand its properties. Processes that release energy in the early universe can distort the CMB spectrum from a blackbody, producing changes to both the chemical potential μ and inducing a characteristic Compton scattering distortion through the Sunyaev-Zel'dovich (SZ) effect y [31–35]. Gravitational energy released in the process of structure formation must distort the spectrum, while numerous models propose other energetic processes in the early universe, such as primordial black holes and variants of dark matter, that could leave traces in the CMB spectrum at detectable levels [36]. Similarly, CMB polarization carries information on reionization and the neutrino mass (via the E-mode component) as well as inflation (via B-modes).

JCAP04(2025)020

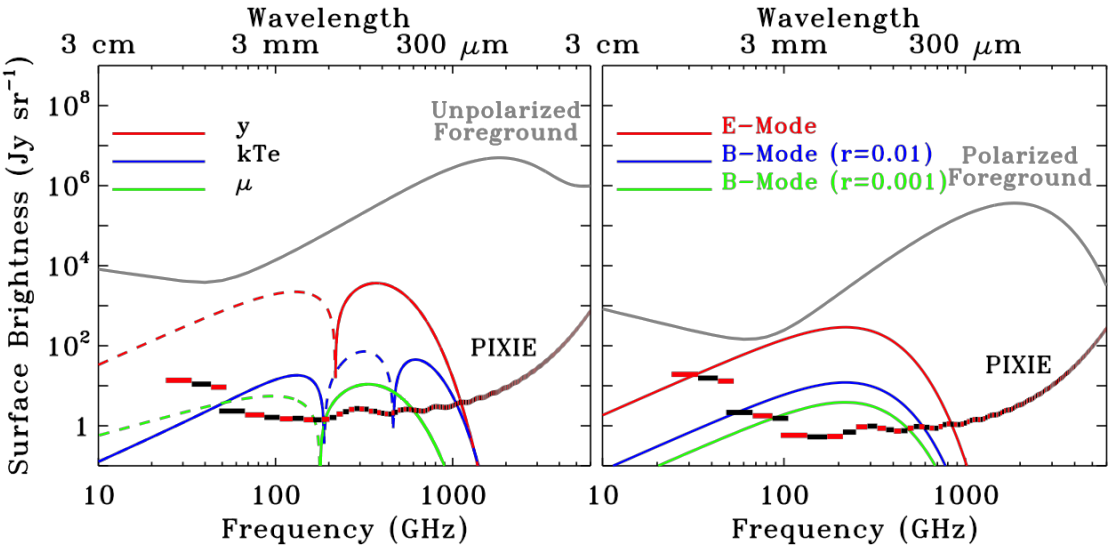

Figure 2. Sensitivity and spectral coverage for the PIXIE baseline 2-year mission in spectral distortions (left) and polarization (right). Predicted cosmological signals are shown for the electron pressure (y) and temperature (kT_e) from structure formation, the dissipation of primordial density perturbations (μ), E-mode polarization from reionization, and B-mode polarization from inflation with tensor-to-scalar ratio $r = 0.01$ and $r = 0.001$. Dashed lines indicate signals with negative amplitude.

Figure 2 compares selected cosmological signals to the median emission from astrophysical foregrounds at high Galactic latitudes. Cosmological signals at amplitudes of a few Jy sr^{-1} are 2–4 orders of magnitude fainter than the foregrounds at all frequencies. Detecting the cosmological signals requires both sensitivity and broad spectral coverage to distinguish the cosmological signals from competing foreground emission.

The Primordial Inflation Explorer (PIXIE) is a proposed space mission to measure the spectrum and polarization of the cosmic microwave background and astrophysical foregrounds on angular scales of 1° and larger [37–39]. Operating from the second Sun-Earth Lagrange point (L2), it would survey the entire sky in intensity and linear polarization at integrated sensitivity of a few Jy sr^{-1} in 300 spectral channels from 28 GHz to 6 THz (figure 2).

PIXIE was first proposed as a NASA medium-class Explorer in 2011 [37]. Previous papers have described the PIXIE detectors [40], optics [41, 42], calibration [38], and systematic error budget [39, 43]. In this paper, we review the PIXIE instrument design, describe changes since the initial 2011 mission concept, and highlight the anticipated scientific results from its baseline 2-year mission. Section 2 describes the updated mission design, sensitivity, and foreground subtraction. Section 3 reviews the principal science goals, updates the predicted sensitivity for cosmological parameters, and provides new forecasts for measurements of the cosmic infrared background, Galactic emission lines, and the star formation rate density at redshifts $z < 5$. Section 4 discusses the limitations of the single-FTS instrument configuration and outlines the sensitivity gains possible with a larger "Super-PIXIE" mission. Separate appendices detail the data sampling and interferogram apodization, outline the principal design features responsible for the sensitivity improvements relative to COBE/FIRAS, and present the full noise curves for the baseline PIXIE mission.

JCAP04(2025)020

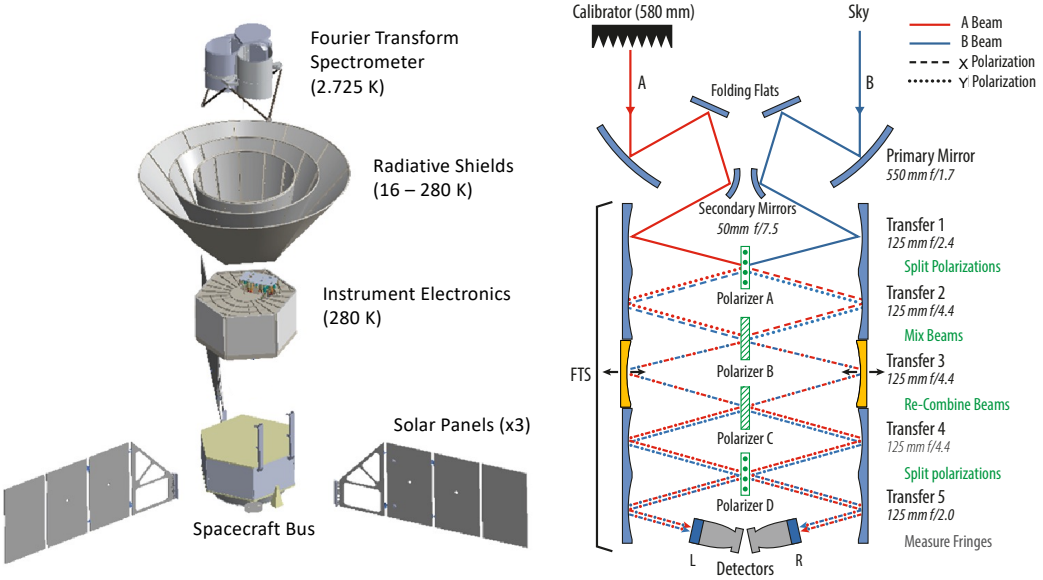

Figure 3. Left: exploded view of the PIXIE observatory. Nested, passively cooled shells surround a polarizing Fourier transform spectrometer, which is actively cooled to 2.725 K to match the CMB monopole emission. Right: PIXIE's optical design measures both intensity and polarization from microwave to THz frequencies. As the central mirror pair moves, the detectors measure a fringe pattern proportional to the Fourier transform of the difference between one linear polarization from beam A and the orthogonal polarization from beam B.

2 PIXIE mission

The PIXIE instrument (figure 3) is a polarizing Fourier transform spectrometer (FTS) with two input ports and two output ports. The input ports are fed by two off-axis telescopes that produce twin beams co-pointed along the spacecraft spin axis. Each telescope has a primary mirror 550 mm in diameter. Folding flats and secondary mirrors route the beams to the FTS while retaining orthogonal polarization alignment between the two beams. Within the FTS a set of five transfer mirror pairs, each imaging the previous mirror to the following one, shuttles the radiation through a series of polarizing wire grids. Polarizer A transmits one polarization and reflects the other, separating each beam into orthogonal polarization states Polarizer B, oriented 45° relative to Polarizer A, mixes the polarization states. A Mirror Transport Mechanism (MTM) moves the central mirror pair ±4 mm to produce an optical phase delay of up to ±15 mm. The phase-delayed beams re-combine (interfere) at Polarizer C. Polarizer D (aligned to Polarizer A) splits the beams again and routes them to two multi-moded concentrators. Each concentrator has a square aperture to preserve linear polarization [41, 42] and contains a pair of orthogonal polarization-sensitive bolometers mounted back-to-back. The square aperture is aligned with respect to the plane of polarization from Polarizer D to enforce symmetry between orthogonal linear polarizations [42]. The four bolometers are cooled to 0.1 K [44] to achieve background-limited sensitivity. The optical spectrum is the Fourier conjugate of the detector's time-ordered data across the mirror sweep. The mirror stroke length sets the optical frequency resolution while the detector sampling rate determines the highest optical frequency.

JCAP04(2025)020

Each of the four detectors measures an interference fringe pattern (interferogram) between orthogonal linear polarizations from the two co-aligned input beams. The spacecraft spins at 1.25 RPM about the beam axis to repeatedly interchange the x and y polarizations on the detectors. The Fourier transform of the observed fringe pattern yields difference spectra

$$\begin{aligned} S(\nu)_{Lx} &= \frac{1}{4}\,[\; I(\nu)_A - I(\nu)_B + Q(\nu)\cos 2\gamma + U(\nu)\sin 2\gamma \;] \\ S(\nu)_{Ly} &= \frac{1}{4}\,[\; I(\nu)_A - I(\nu)_B - Q(\nu)\cos 2\gamma - U(\nu)\sin 2\gamma \;] \\ S(\nu)_{Rx} &= \frac{1}{4}\,[\; I(\nu)_B - I(\nu)_A + Q(\nu)\cos 2\gamma + U(\nu)\sin 2\gamma \;] \\ S(\nu)_{Ly} &= \frac{1}{4}\,[\; I(\nu)_B - I(\nu)_A - Q(\nu)\cos 2\gamma - U(\nu)\sin 2\gamma \;]\;, \end{aligned} \tag{2.1}$$

where I, Q, and U are the Stokes polarization parameters, γ is the spacecraft spin angle, and $S(\nu)$ denotes the synthesized frequency spectrum with bins centered at frequencies ν set by the fringe sampling. A and B refer to the two input beams, while L and R refer to the left and right detector concentrators.

PIXIE carries a full-aperture blackbody calibrator to provide an absolute reference source [38]. The calibrator can be deployed to fully cover either beam, or be stowed so both beams view the sky. When both beams view the sky, the instrument nulls unpolarized emission, so the fringe pattern encodes only the frequency spectrum of polarized emission. When the calibrator covers either beam, the fringe pattern encodes information for both polarization and the absolute intensity of sky emission. Interleaving observations with the calibrator stowed or deployed allows for the straightforward transfer of the absolute calibration scale to linear polarization while providing a valuable cross-check of the polarization solutions obtained in each mode. To control stray light, all internal surfaces except the active optical elements are coated with a microwave absorber [45, 46] forming a blackbody cavity nearly isothermal with the sky. Active thermal control maintains the telescope, FTS, and surrounding walls within a few mK of the 2.725 K CMB temperature, reducing thermal gradients within the instrument to minimize effects of internal absorption or reflection [38, 39, 43].

PIXIE observes from a thermally-stable Sun-Earth Lagrange Point 2 (L2) halo orbit. The spacecraft spins about the instrument optical boresight at 1.25 RPM while simultaneously scanning the boresight through a 5.12 hour period great circle perpendicular to the Earth-Sun line (figure 4). The annual orbital motion precesses the great-circle orientation to achieve full-sky coverage every six months. The 2-year baseline mission produces 4 redundant full-sky maps for jackknife comparison.

Data sampling is synchronous with the instrument spin, with the mirror stroke, spacecraft spin, and great-circle scan maintained in a fixed ratio driven by a single master clock. Several scales are relevant. The multi-moded optics produce a circular tophat beam[1] with diameter 2.65°. The sky spectra are sorted using the HEALPIX pixelization at resolution `NSIDE=64` [47]; the resulting 0.9° pixel size over-samples the beam. The MTM produces an interferogram every 3 seconds, the spacecraft rotates about the beam axis every 48 seconds, and each great circle scan requires 5.12 hours (384 rotations). During each great circle scan, each pixel

[1]The window function for the tophat beam may be approximated by a Gaussian beam with 1.65° full width at half maximum.

JCAP04(2025)020

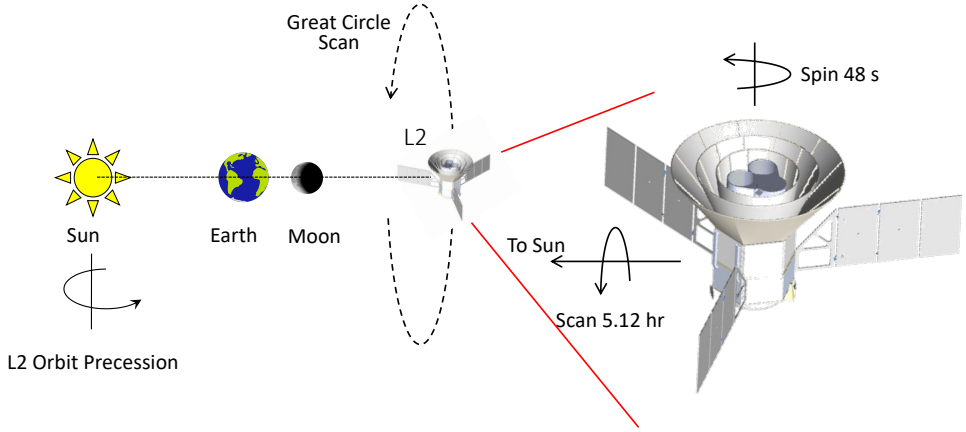

Figure 4. PIXIE will observe at the Sun-Earth L2 point. The spacecraft spins about the beam boresight while simultaneously scanning the beams in a great circle perpendicular to the sun line. The scan pattern maps the full sky every 6 months.

acquires data from interferograms at 16 evenly-spaced spin angles. Appendix A details the data sampling and apodization of the sampled interferograms.

The baseline 2-year mission assumes that 45% of observing time is spent with the calibrator deployed (sensitive to spectral distortions and polarization) and 45% with the calibrator stowed (sensitive to polarization only). The remaining 10% conservatively accounts for time not used for science observations (MTM turnaround at the end of each stroke, thermal settling after setpoint changes, etc). The calibrator deployment schedule can be altered during the mission to provide more or less integration time in each mode. Mission operations further assume observations at two different MTM stroke lengths, providing additional sensitivity to low-frequency foregrounds.

The PIXIE instrument and mission have evolved since the initial 2011 concept [37]. The 2011 version assumed observations from a 660 km polar sun-synchronous low-Earth orbit, while the current version will observe from the second Sun-Earth Lagrange point. The L2 orbit improves thermal stability for the observatory, reduces emission from the Earth and Moon to negligible levels, and by decoupling the great circle scan motion from the low-Earth orbital period simplifies synchronization of the interferogram mirror stroke, observatory spin, and great circle scan. Within the instrument, the optical path through the FTS has been shortened, replacing the previous corner reflector MTM with a pair of powered mirrors. The 2011 concept assumed that all observations would use the same MTM stroke, and thus the same set of frequency channels. To obtain additional low-frequency channels, the current design assumes a combination of observations with short and long MTM strokes (section 2.1). The resulting sensitivity curves correct a factor-of-two error from the 2011 estimate (eq. (2.4)) and now include the frequency-dependent effects of the reflective backshort in the detector integrating cavity. The baseline mission has been shortened from 4 years to 2 years, based on the observing time required for a definitive measurement of the cosmological distortions from Compton scattering.

JCAP04(2025)020

2.1 Sensitivity

The noise equivalent power (NEP) from photon arrival statistics in a single linear polarization at the detector is given by

$$\mathrm{NEP}^2 = 2\frac{A\Omega}{c^2}\frac{(k_B T)^5}{h^3}\int \frac{x^4 dx}{e^x - 1}\left(1 + \frac{\alpha\epsilon f}{e^x - 1}\right)(\alpha\epsilon f) \tag{2.2}$$

where A is the detector area, Ω is the detector solid angle, ν is the optical observing frequency, T is the physical temperature of the source, ϵ is the emissivity of the source, h is the Planck constant, k_B is the Boltzmann constant, c is the speed of light, $x = h\nu/k_B T$ is the dimensionless frequency, α is detector absorptivity, and f is the power transmission through the optics to the detector [48]. The prefactor 2 corresponds to a single linear polarization. For non-thermal sources, it is convenient to express the NEP in terms of the optical power P_ν,

$$\mathrm{NEP}^2 = \int d\nu \left(\alpha f h\nu P_\nu + \frac{\alpha^2 f^2 P_\nu^2}{N_m}\right), \tag{2.3}$$

where $N_m = A\Omega/\lambda^2$ is the number of electromagnetic modes accepted by the detector [49]. Since the detected signal varies linearly with etendue $A\Omega$ while the noise varies as $\sqrt{A\Omega}$, the signal-to-noise ratio increases as the square root of the etendue. The PIXIE detectors each have active absorber area 1.69 cm^2 and etendue 4 cm^2 sr. The detector absorbing structure is degeneratively doped to sheet resistance 377 $\Omega/\square$, matching the impedance of free space. The detectors are mounted within an integrating cavity with a reflective backshort 0.689 mm behind the detectors. The backshort increases the detection efficiency for the CMB component to $\alpha = 0.57$, while the efficiency at frequencies much higher than the CMB peak averages $\alpha = 0.52$.

The photon noise depends on the optical power incident on the detector, which for PIXIE is dominated by the CMB monopole or the calibrator. The FTS optics provide throughput $f = 0.9$ from the FTS input port to the detectors [50]. The waveguide cutoff of the concentrators limits the throughput at frequencies below 12 GHz, while several design elements combine to limit the high-frequency response. The 30 μm pitch of the micro-machined detector absorbing strands acts as a single-pole low-pass filter at wavelength 60 μm. Two roughened mirrors within each telescope scatter short wavelengths out of the beam and onto the blackened walls, producing low-pass filters with poles at wavelength 200 μm. The wire grid polarizers become ineffective at wavelengths comparable to wire pitch; these act as a set of four 60 μm single-pole low-pass filters to reduce the fringe amplitude (signal) but do not affect the photon noise. Similarly, the differential path length for rays at the FTS mirror centers versus edges washes out the fringes at short wavelengths, again reducing signal while not affecting noise.

We estimate the optical load and photon NEP at the detector using eq. (2.2), including contributions from the CMB 2.725 K monopole, Galactic synchrotron, free-free, and thermal dust emission, the cosmic infrared background, and local zodiacal emission. The top panel of figure 5 shows the differential contribution to the photon NEP as a function of optical frequency. The bottom panel shows the integrated photon NEP as a function of the highest

JCAP04(2025)020

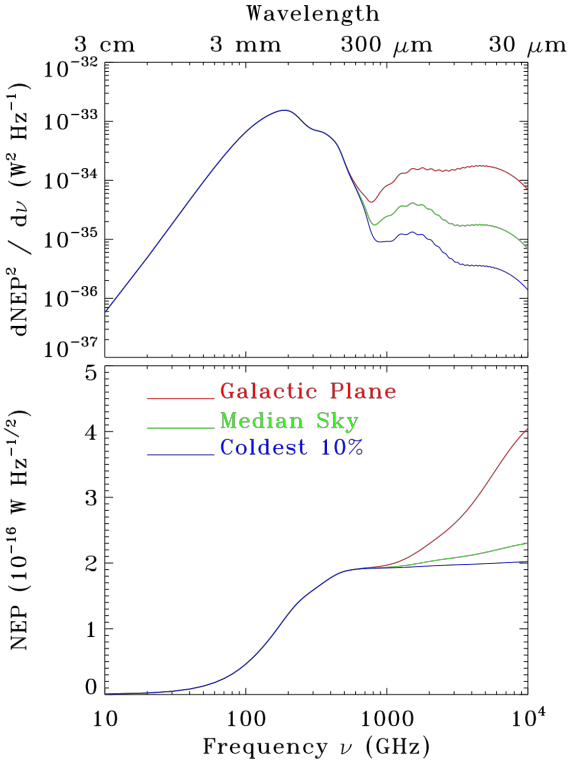

Figure 5. The photon noise equivalent power through the PIXIE optics is shown for different parts of the sky. (top) The NEP integrand (eq. (2.2)) is dominated by the CMB at mm wavelengths, with minor contribution from Galactic dust, the CIB, and zodiacal emission if the passband extends to shorter wavelengths. Colors compare the photon noise for different lines of sight through the Galaxy. (bottom) NEP as a function of highest optical frequency (integral of top panel). Scattering filters on the optics allow the optical passband to extend to 6 THz without significant noise penalty over most of the sky.

optical frequency observed. The scattering filters limit the high-frequency contribution from foreground components so that the photon NEP is dominated by the CMB monopole or blackbody calibrator. Thermal dust emission is a significant noise source only near the Galactic plane. Extending the optical passband from 600 GHz to 6 THz increases the photon NEP by 16% for the median sky brightness, and only 5% for the darkest 10% of the sky, compared to the NEP from the CMB alone. At the median sky brightness, the photon NEP is $2.2 \times 10^{-16}\,\mathrm{W}/\sqrt{\mathrm{Hz}}$. For the corresponding optical load of 139 pW and a detector substrate temperature of 100 mK, the PIXIE detector adds phonon NEP $1.5 \times 10^{-16}\,\mathrm{W}/\sqrt{\mathrm{Hz}}$ in quadrature with the photon noise for a total NEP $= 2.7 \times 10^{-16}\,\mathrm{W}/\sqrt{\mathrm{Hz}}$.

The NEP and data sampling determine the noise in the interferograms,

$$\delta P_k = \frac{\mathrm{NEP}}{\sqrt{2\delta t_k}}\,, \tag{2.4}$$

where δt_k is the integration time for the k^{th} interferogram sample and the factor of 2 accounts for the conversion between the frequency and time domains. After Fourier transformation,

JCAP04(2025)020

the noise in each synthesized channel is given by the Fourier sum

$$\delta P_\nu = \frac{1}{N_s} \sum_k \delta P_k \exp(i2\pi\nu Z_k/c/N_s)\,, \tag{2.5}$$

where N_s is the number of samples and Z_k is the optical phase delay of the k^{th} sample. The Fourier-transformed noise may in turn be referred to the surface brightness on the sky,

$$\delta S(\nu) = \frac{\delta P_\nu}{N_B\, A\Omega\, \Delta\nu\, (\alpha f)}\,, \tag{2.6}$$

where $\Delta\nu$ is the bandwidth of the synthesized frequency channels after the Fourier transform. The transmission through the optics f includes the frequency-dependent signal loss from signal dispersion and the polarizer grid efficiency, as well as the optical scattering filters. The factor N_B accounts for the number of beams on the sky: $N_B = 1$ for measurements when the calibrator blocks one beam (spectral distortions) while $N_B = 2$ for measurements with the calibrator stowed so that both beams observe the sky (polarization).

The MTM moves at constant physical velocity: for a fixed total integration time, the integration time δt_i for each data sample thus scales linearly with the desired channel width, while the noise in the synthesized spectral channels scales as $1/\Delta\nu$ (eqs. (2.4)–(2.6)). The optimum channel width depends on the sky signal. For line emission, it is desirable to match the channel width to the width of the line profile; broader channels wash out emission from the line. For continuum emission the opposite is true: the channel width should be as large as possible consistent with retaining sufficient channels for any necessary spectral fitting. Since the signal is coherent while the noise is not, the signal to noise ratio for continuum emission will improve as $\sqrt{\Delta\nu}$ when integrated over channels.

The PIXIE channel width is determined by the need to separate cosmological signals from competing foregrounds (section 2.2). Channel widths $\Delta\nu \sim 20\,\mathrm{GHz}$ providing spectral resolution $\nu/\Delta\nu \sim 15$ near the CMB peak at 270 GHz do not provide sufficient resolution to fit multiple foreground components (synchrotron, free-free, and anomalous microwave emission) at frequencies below 70 GH, while channel widths $\Delta\nu < 10\,\mathrm{GHz}$ appropriate for low-frequency foregrounds degrade the sensitivity to CMB signals at higher frequencies. As a compromise, PIXIE spends 70% of the observing time in "short-stroke" mode using broad channel widths for continuum CMB signals, and 30% in "long-stroke" mode with narrow widths for low-frequency foregrounds. It is convenient to set all channel widths commensurate with the CO J=1-0 line at 115.3 GHz within the Galaxy, $\Delta\nu = \nu_{\mathrm{CO}}/M$ so that every M^{th} channel is centered on a Galactic CO line. For measurements of spectral distortions, PIXIE will use $M = 6$ ($\Delta\nu = 19.2\,\mathrm{GHz}$) and $M = 12$ ($\Delta\nu = 9.6\,\mathrm{GHz}$). The free-free and anomalous microwave foreground emission are not polarized at relevant levels, allowing use of wider channel widths $M = 3$ ($\Delta\nu = 38.4\,\mathrm{GHz}$) and $M = 6$ ($\Delta\nu = 19.2\,\mathrm{GHz}$) for polarization measurements. Appendix C lists the resulting channel sensitivities.

2.2 Foreground subtraction

Foreground emission from both galactic and extragalactic sources degrades PIXIE's sensitivity to cosmological signals. Figure 6 compares the principal foregrounds to the spectral

JCAP04(2025)020

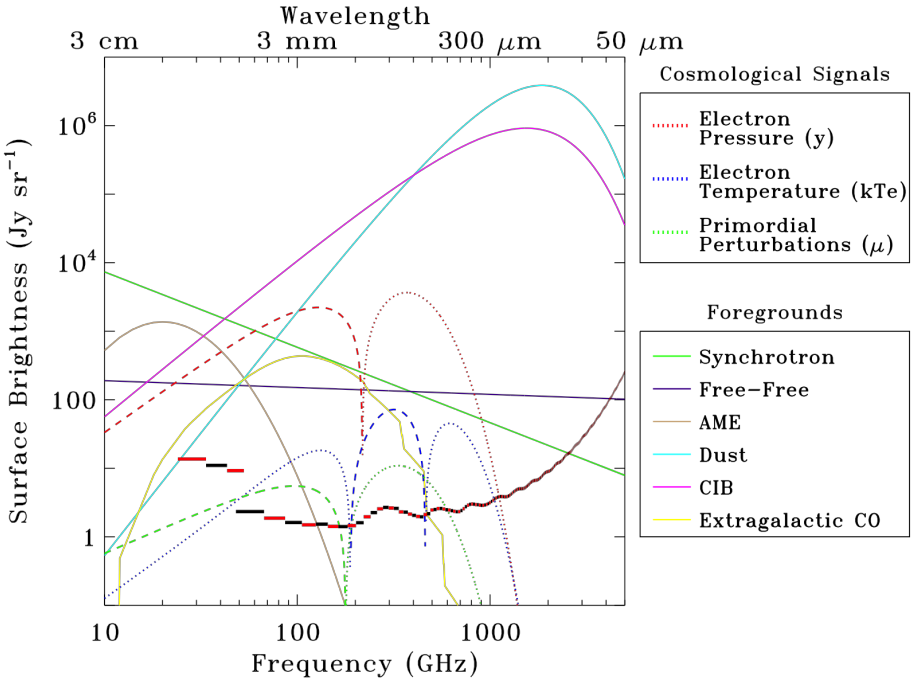

Figure 6. Solid lines show the spectra of the principal foregrounds at the median amplitude for Galactic latitude $|b| > 20°$. Dotted and dashed lines show the cosmological signals, with negative amplitudes dashed. The black/red curve shows the PIXIE noise in each spectral channel for the baseline 2-year mission, averaged over the cleanest 70% of the sky. The rise in noise at frequencies below 40 GHz reflects the smaller fraction of observing time spent with the MTM in long-stroke mode. PIXIE's sensitivity to cosmological signals is limited by competing emission from astrophysical foregrounds (see text).

distortions from structure formation and the dissipation of primordial density perturbations. Following [51], we assess the impact of foreground emission using the mission noise curves from this paper in a parametric fit to the cosmological signals and foreground emission. The 11-parameter foreground model treats thermal dust emission and the cosmic infrared background as separate modified blackbodies, $I_\nu \propto B_\nu(T)\nu^\beta$ and fits the amplitude, temperature, and spectral index of each component. We model synchrotron as a power-law $I_\nu \propto \nu^\beta$ and fit the amplitude and spectral index. We fix the spectra of the remaining foregrounds (free-free, anomalous microwave emission, and integrated extragalactic CO) and simply fit the amplitude for each component. An additional 4 parameters fit the CMB monopole temperature T_0, the electron pressure y, electron temperature kT_e, and the chemical potential μ. At frequencies above ∼3 THz, the spectral energy distribution of the dust and CIB become more complicated; we thus report spectral distortion limits using only freqeuncies below 3 THz (although higher frequencies may inform the foreground fitting and are useful for other science goals).

Table 1 shows the signal to noise ratio for the cosmological signals estimated using a Fisher analysis of the noise levels integrated over the cleanest 70% of the sky. We adopt fiducial values $y = 1.77 \times 10^{-6}$ and $kT_e = 1.245\,\mathrm{keV}$ predicted for the integrated signal from Compton scattering from groups and clusters of galaxies [52] and $\mu = 2 \times 10^{-8}$ for the

JCAP04(2025)020

Mission	Foreground	y	kT$_e$	μ^a	y	kT$_e$	μ
Baseline	No foregrounds	4853	85	—	3101	80	2.9
	No priors	103	6.2	—	18	1.8	0.02
	10% priors	179	8.3	—	108	7.1	0.09
	1% priors	202	9.6	—	159	8.1	0.43
Extended	No foregrounds	16 000	282	—	10 200	265	9.7
	No priors	342	20	—	61	6.0	0.06
	10% priors	564	27	—	213	19	0.15
	1% priors	617	29	—	474	25	0.73

[a]Not fitted.

Table 1. Predicted signal to noise ratio for spectral distortions.

dissipation of primordial density perturbations from a power-law distribution consistent with the scale-invariant spectrum seen in primary CMB anisotropies [53]. Results are shown for the baseline PIXIE mission (two years of observations with 45% of observations devoted to spectral distortions, yielding 7.6 months of integration for monopole distortions within the cleanest 70% of the sky) as well as an extended mission with a total of 7 years integration time in spectral distortion mode.

In the absence of foreground emission, the baseline PIXIE mission would detect the cosmological signals at high confidence: 3101 standard deviations for y, 80 standard deviations for kT_e, and 2.9 standard deviations for μ. The need to identify and subtract foreground emission degrades these values. A minimal fit using just the PIXIE mission data with no foreground priors provides a robust detection of the predicted Compton signal (18 standard deviations for y and 2 standard deviations for kT_e) but falls short of a detection of the chemical potential predicted in the standard ΛCDM model from Silk damping of a power-law distribution of primordial density perturbations (section 3.2). We investigate the ability to improve these limits by repeating the analysis while placing priors on selected foreground parameters. PIXIE data at frequencies above ∼600 GHz place tight constraints on the amplitude and spectra of the thermal dust and CIB foregrounds and are unlikely to be superseded by other data. The sensitivity at lower frequencies is limited by the fixed channel width imposed by Fourier transform spectroscopy (section 2.1) and can be improved by including information from measurements at lower frequencies. We repeat the Fisher analysis placing Gaussian priors of 10% or 1% on the synchrotron and free-free parameters. Placing 10% priors on the low-frequency foregrounds provides a five-fold improvement in the sensitivity to cosmological signals, but still falls short of a detection for the minimal μ distortion from a ΛCDM cosmology. Even the combination of tighter (1%) priors over a 7-year extended mission produces uncertainty larger than the predicted chemical potential distortion. Obtaining additional sensitivity to low-frequency foregrounds would require additional instrumentation to reduce photon noise at frequencies below ∼150 GHz, extend measurements to frequencies below 30 GHz, or both. section 4 discusses possible enhancements for such a "Super-PIXIE" design.

Covariance between the y and μ distortions affects the uncertainties for both parameters. Table 1 lists the predicted signal to noise ratios with and without fitting for μ. Absent

JCAP04(2025)020

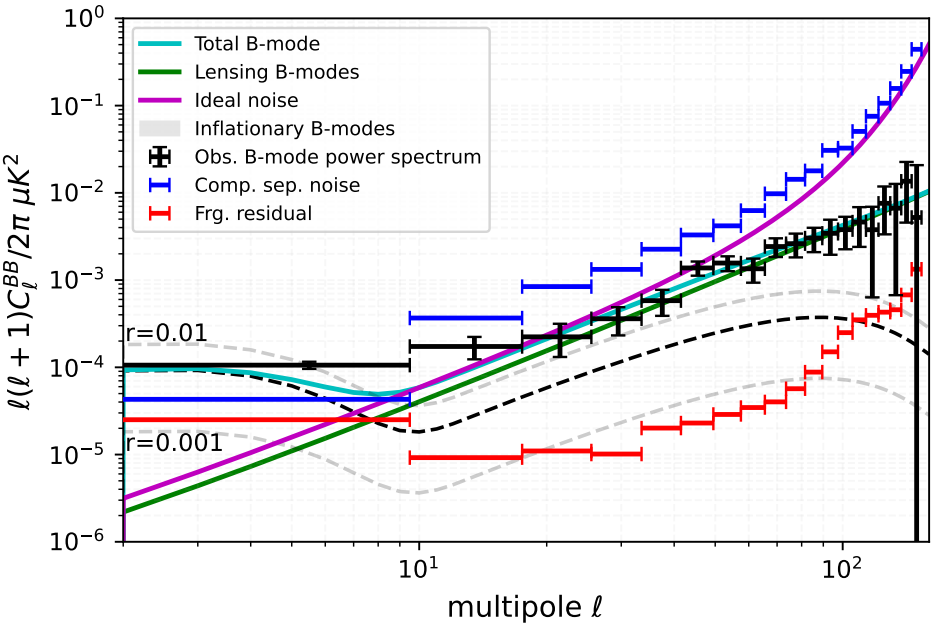

Figure 7. Simulation results of NILC foreground decomposition for the PIXIE baseline mission. The dashed line shows the $r = 5 \times 10^{-3}$ inflationary signal used for the simulation.

a significant detection for μ, a parametric fit excluding the μ distortion improves the uncertainties for both the electron pressure y and temperature kT_e, particularly for the case with no foreground priors.

Foreground subtraction in polarization is less complex, as only the synchrotron and thermal dust foregrounds are expected to have significant polarization. Figure 7 shows PIXIE's polarization capability using a Needlet Internal Linear Combination (NILC) component separation [54–57]). We generate a noiseless full-sky foreground model using the Python Sky Model d1s1 variant [58] and add cosmological signals from E-modes, lensing B-modes, and primordial B-modes at amplitude $r = 5 \times 10^{-3}$. All signals are convolved with a 1.6° full width at half maximum Gaussian beam before adding noise within each PIXIE frequency channel. We complement the PIXIE frequency coverage using the Planck polarization maps, then evaluate the resulting sky maps on the cleanest 70% of the sky, using a Fisher analysis to estimate the uncertainty $\sigma(r)$ and a likelihood analysis to determine the 95% confidence upper limit r_{95} [59]. As with spectral distortions, the foreground subtraction increases the effective noise with noise amplitude (after component separation) worse by a factor 1.8 in amplitude or 3.2 in power. Foreground residuals are sub-dominant to the noise and create negligible bias.

Gravitational lensing of the dominant E-mode polarization creates an additional cosmological foreground for measurements of B-mode polarization from primordial tensor perturbations. The power spectrum for PIXIE B-mode noise is close to the amplitude for the un-corrected lensing foreground; roughly 70% of the weight for B-mode polarization analysis results from multipoles $\ell \leq 10$ where the primordial B-mode signal pulls away from the lensing foreground. The PIXIE 1.6° angular resolution does not permit de-lensing using only PIXIE data; any de-lensing must use external data (e.g. from CIB anisotropy or other CMB missions). Table 2

JCAP04(2025)020

Mission	$A_{\rm lens}$	$\sigma(r)$ $\times 10^3$	FG Bias $\times 10^3$	r_{95} $\times 10^3$
Baseline	0.3	0.89	0.39	2.54
	0.5	0.91	0.39	2.63
	1.0	0.98	0.41	2.86
Extended	0.3	0.30	0.06	0.75
	0.5	0.33	0.07	0.85
	1.0	0.40	0.08	1.07

Table 2. PIXIE B-mode polarization limits.

shows PIXIE B-mode limits for different levels of de-lensing, where the parameter $A_{\rm lens}$ shows the amplitude of the remaining (un-corrected) lensing signal. If no de-lensing is performed ($A_{\rm lens} = 1$), the baseline PIXIE mission achieves $\sigma(r) = 0.98 \times 10^{-3}$ for a 95% confidence upper limit $r_{95} = 2.86 \times 10^{-3}$. Residual foregrounds contribute a bias $r_{\rm fg} = 0.41 \times 10^{-3}$, small compared to the noise. Neither the B-mode uncertainty nor the foreground residuals depend significantly on the assumed level of de-lensing. The fraction of mission observations devoted to polarization (calibrator stowed so that both beams view the sky) can be changed throughout the mission. An extended mission with a total of 7 years of polarization observation would improve the B-mode limits to $\sigma(r) = 0.4 \times 10^{-3}$ and $r_{95} = 1.1 \times 10^{-3}$, with foreground bias $r_{\rm fg} = 0.08 \times 10^{-3}$. With modest delensing ($A_{\rm lens} = 0.5$), the 95% confidence upper limits improve to 2.6×10^{-3} for the baseline mission and 0.9×10^{-3} for an extended mission.

PIXIE will also measure E-mode polarization to constrain the optical depth to reionization. A similar NILC decomposition using PIXIE and Planck data over the cleanest 70% of the sky provides uncertainties $\sigma(\tau) = 2.6 \times 10^{-3}$ for the baseline mission and $\sigma(\tau) = 2.5 \times 10^{-3}$ for an extended mission. These uncertainties compare well to the cosmic-variance limit 2.03×10^{-3}.

The above forecasts assume a simple foreground model (d1s1) from widely used PySM sky model. Recent Planck data suggest that variation of the thermal dust spectral across the sky may be larger than assumed in this model. To investigate the impact of additional complexity in the foreground model, we have run the NILC code on more recent models implemented in PySM3, which use template maps and statistics of foreground spectra from Planck public data release 3 [57, 60]. The medium complexity model (PySM3 d10s5) is similar to the baseline low-complexity model except that the dust model d10 shows significantly more spatial variability of the dust spectrum in mid-to-high Galactic latitudes. The high-complexity sky model (PySM3 d12s7a2) adds 2% fractional polarization for AME, spectral curvature for synchrotron emission, and adopts a 6-layer multi-component model for polarized dust emission [61]. The medium and high complexity models are expected to be valid only within the limited frequency range 1–1000 GHz. We thus restrict the NILC analysis to PIXIE channels below 1000 GHz, but include an external channel with beam width and sensitivity comparable to WMAP K band as an additional tracer of polarized synchrotron.

Over the cleanest 70% of the sky, the medium or high complexity models degrade the sensitivity $\sigma(r)$ by a factor 2–3 compared to the baseline model. The reduced sensitivity is driven almost entirely by complexity in the dust model. Although use of the PySM3

JCAP04(2025)020

Signal	Parameter	Fiducial Value	68% CL Uncertainty	
			Baseline	Extended
Electron Pressure	y	1.77×10^{-6}	1.6×10^{-8}	8.3×10^{-9}
Electron Temperature	kT_e	1.245 keV	0.17 keV	0.065 keV
Primordial Silk Damping	μ	2×10^{-8}	2.2×10^{-7}	1.3×10^{-7}
Inflation	r	10^{-3} — 10^{-2}	0.9×10^{-3}	0.3×10^{-3}
Reionization	τ	0.05	2.6×10^{-3}	2.5×10^{-3}
Neutrino Mass	$\sum m_\nu$	>58 meV	13.1 meV	13.0 meV

Note. Parameter uncertainties shown after foreground marginalization assuming weak 10% priors on synchrotron and free-free parameters and 50% delensing.

Table 3. Cosmological parameter limits.

models restricts analysis to frequencies below 1000 GHz, PIXIE will produce 52 frequency channels sensitive to polarized dust at frequencies 1–3.5 THz, with median signal-to-noise ratios 25–600 in individual high-latitude voxels within this frequency range. Observations with the calibrator deployed provide additional, independent data for both polarized and unpolarized foregrounds. A full treatment of foreground modeling with PIXIE is beyond the scope of this paper and is deferred to a future work.

3 Science goals

PIXIE will survey the full sky at levels of a few hundred Jy per beam for each of the Stokes I, Q, and U parameters in 300 spectral channels from 28 GHz to 6 THz, reaching limits of a few Jy sr^{-1} for signals averaged over broad regions of the sky. Table 3 lists the resulting sensitivity to selected cosmological parameters. We discuss below the science goals enabled by these measurements.

3.1 Inflation

CMB polarization provides a test of inflation through the B-mode gravitational wave signal generated during the inflationary epoch [62–69]. Figure 8 compares the PIXIE sensitivity (after foreground component separation, section 2.2) to the B-mode power spectrum at values $r = 0.01$ predicted by the simplest models and $r = 0.001$ for a range of more complex models. The 2-year baseline mission spends 45% of the total time observing polarization, and achieves 68% confidence uncertainty $\sigma(r) = 0.9 \times 10^{-3}$ and 95% confidence upper limit $r_{95} = 2.6 \times 10^{-3}$, providing robust detection for signals at levels $r \sim 0.01$. An extended mission with a total of 7 years integration in polarization improves these limits to $\sigma(r) = 0.3 \times 10^{-3}$ and 95% confidence upper limit $r_{95} = 0.9 \times 10^{-3}$ to constrain multi-field models.

3.2 Primordial density perturbations

Primary CMB anisotropies map a nearly scale-invariant power spectrum of primordial density perturbations on co-moving scales > 1 Mpc. Although inflation provides a cogent explanation

JCAP04(2025)020

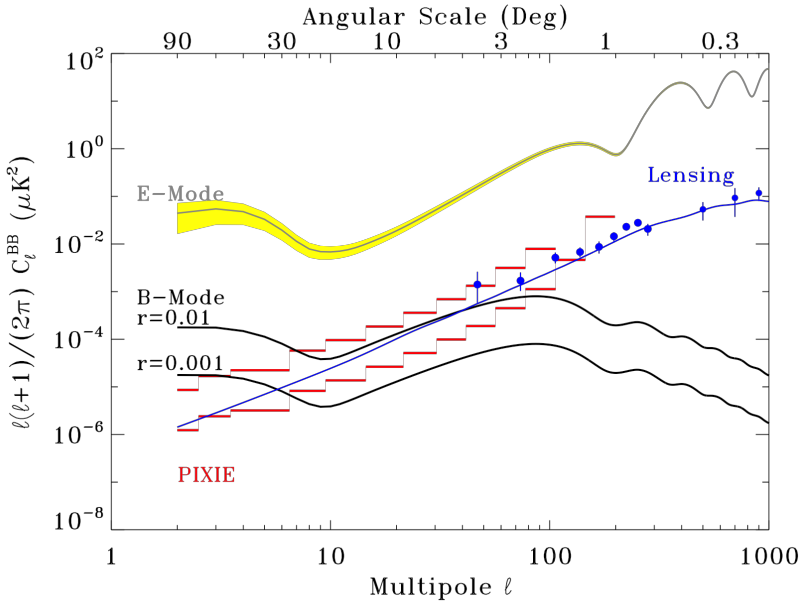

Figure 8. Power spectra for E-mode and B-mode polarization compared to the PIXIE sensitivity. The shaded yellow region shows the E-mode cosmic variance. The red lines show the PIXIE noise after foreground component separation for the baseline (upper curve) and extended (lower curve) missions. Blue points show current B-mode detections of the lensing foreground.

for the observed large-scale structure in the early Universe, there is as yet no generally-accepted model of the underlying physics and no compelling evidence for any specific inflationary model. Spectral distortions provide an independent window to inflation and the primordial universe. Inflation may or may not be the correct model for the primordial universe, but primordial density perturbations exist and source distortions from the CMB blackbody spectrum. On comoving scales below 1 Mpc, photon diffusion (Silk damping) erases the primordial fluctuations and transfers their energy to the CMB, creating a chemical potential (μ-distortion) whose amplitude depends on the amplitude of the density perturbations at these scales [53, 70–73]. PIXIE constraints on μ probe the amplitude of density fluctuations on physical scales 3–4 orders of magnitude smaller than can be measured with primary CMB anisotropy.

If the scale-invariant power spectrum observed in primary CMB anisotropies persists to these smaller scales, the standard ΛCDM cosmology predicts spectral distortion $\mu \sim 2 \times 10^{-8}$ [53]. Foreground subtraction limits PIXIE to 95% confidence limits $|\mu| < 9 \times 10^{-8}$ for the baseline mission and $|\mu| < 5 \times 10^{-8}$ for an extended mission, assuming 1% low-frequency foreground priors (table 1). PIXIE improves the COBE/FIRAS distortion limit $|\mu| < 9 \times 10^{-5}$ [25] by 3 orders of magnitude, providing new constraints on the amplitude of primordial density perturbations at wavenumber $k = 1{-}10^6\,\mathrm{Mpc}^{-1}$ (figure 9). Upper limits at this level constrain models of inflation, independent of B-mode polarization [74–76].

PIXIE is not expected to detect the damping signal from the ΛCDM cosmology; conversely, any positive detection would point to physics beyond the standard model. Primordial black holes provide an example. Supermassive black holes (SMBHs) with mass $10^8{-}10^9\,M_\odot$ have been observed at the centers of most galaxies, but the detection of gravitational radiation

JCAP04(2025)020

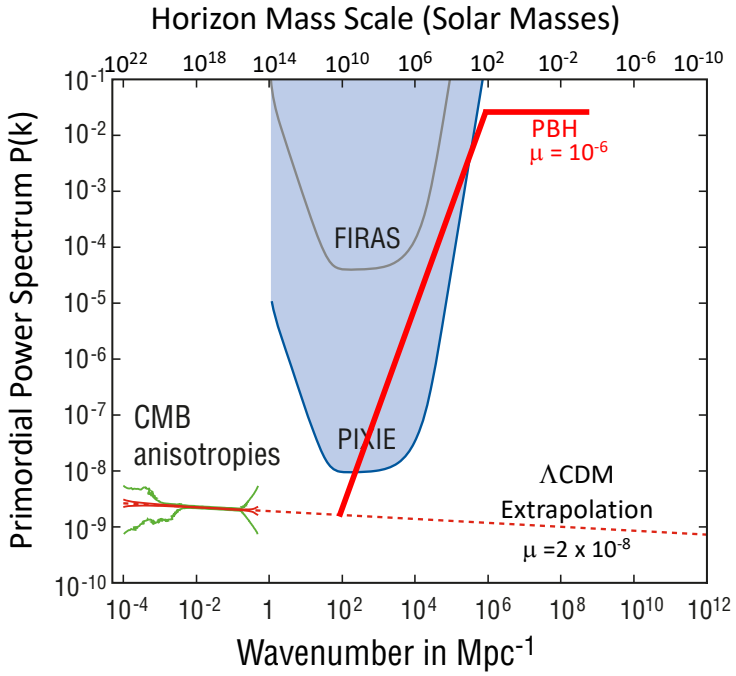

Figure 9. Limits to the amplitude of primordial density perturbations derived from Silk damping (μ distortions). Dissipation of primordial density perturbations in ΛCDM predicts a μ-distortion just below PIXIE's foreground-marginalized sensitivity. Any detection by PIXIE requires new physics, such as the increased power needed to seed primordial black holes (thick red line; see text).

from a population of colliding solar-mass ($1-100\,M_\odot$) BHs was unexpected [77]. Although the rate of detection clearly supports a current population of such BHs, their origin and evolution are unknown. They may represent a population of primordial black holes (PBHs) created as sufficiently-massive primordial density perturbations entered the casual horizon and collapsed. No existing measurement directly constrains the primordial power at the relevant horizon scales. Direct collapse of $1-100\,M_\odot$ perturbations requires power $P\sim 0.01$ at wavenumbers $10^6 < k < 10^8\,\mathrm{Mpc}^{-1}$, some 7 orders of magnitude above the level predicted in ΛCDM from the power observed at scales $k < 1\,\mathrm{Mpc}^{-1}$ by primary CMB anisotropies. The amplitude of density perturbations cannot jump arbitrarily, but must smoothly transition from the ΛCDM value to the much higher amplitude needed for black hole collapse. Figure 9 shows a simple toy model, in which the power spectrum $P(k)$ transitions as k^2 from $P\sim 10^{-9}$ at $k\sim 10^2$ to $P\sim 10^{-1}$ at $k\sim 10^6$ to source a population of ($1-100\,M_\odot$) BHs. Although the perturbations directly responsible for seeding BH collapse do not distort the CMB spectrum, perturbations within the transition region create a detectable signal $\mu\sim 10^{-6}$.

Primordial perturbations will also source a stochastic background of gravitational waves. Enhanced power in primordial density perturbations has been suggested as a possible source for the nHz gravitational wave background detected by pulsar timing measurements [78–81]. Power sufficient to produce the observed pulsar timing signal would distort the CMB spectrum at levels up to $\mu\sim 5\times 10^{-7}$ [76, 82]. Distortions at this level would be detectable by PIXIE.

JCAP04(2025)020

3.3 Particle physics

The neutrino is the only Standard Model particle whose mass is unknown. Measurements of E-mode polarization enable detection of the neutrino mass. Neutrinos affect the growth of structure: massive neutrinos cannot cluster on physical scales smaller than their free-streaming length, suppressing the growth of structure on these scales. Gravitational lensing from CMB and optical surveys determines the amplitude of current structure in our universe, but determining the growth of structure requires knowledge of the primordial amplitude as well. Primary CMB anisotropy only determines the primordial amplitude within ∼1% uncertainty due to scattering at reionization. PIXIE's nearly cosmic-variance limited measurement of the reionization optical depth (section 2.2) would remove this limiting uncertainty to enable a determination of neutrino mass to 4 standard deviation precision [83].

Dark matter (DM) provides a more exotic test of particle physics. The long-favored weakly interacting massive particles (WIMP) scenario is seeing increased pressure from both direct detection experiments and tests for supersymmetry in particle colliders, suggesting instead more exotic scenarios such as axionic DM [84, 85] or PBHs [86]. PIXIE's spectral distortion limits constrain electromagnetic interactions between dark matter and standard-model particles from DM decay annihilation and scattering [87]. Spectral distortions from DM decay depend on the lifetime and abundance of the (excited) DM state. The temperature/velocity-dependence of the DM annihilation cross-section strongly affects annihilation signals, with spectral distortions being particularly valuable for p-wave annihilation [88]. Since the dark matter number density scales as 1/mass, spectral distortions from DM annihilation or scattering are sensitive to low masses. PIXIE 95% confidence limits $|\mu| < 5 \times 10^{-7}$ from the baseline mission restrict Majorana annihilations to mass $m_\chi > \sim 300\,\mathrm{keV}$ [89].

3.4 Structure formation

PIXIE will determine the average pressure and temperature of free electrons in the post-recombination universe, providing critical input for numerical simulations of galaxy formation. Current simulations [90–92] employ a range of parameters for feedback, which couples the gravitational physics of large-scale structure to the non-linear hydrodynamics on smaller (galaxy) scales. Energy injected into circumgalactic and intracluster gas from active galactic nuclei and supernovae plays a critical but poorly-understood role in galaxy formation. Feedback processes shut off star formation in galaxies, heating and expelling gas into the intergalactic medium. The electrons in this gas distort the CMB spectrum via the thermal Sunyaev-Zel'dovich (tSZ) effect. The temperature of this gas ($10^5 - 10^6\,\mathrm{K}$) is sufficiently high to generate non-zero relativistic corrections to the tSZ signal [52, 90]. Assuming weak 10% priors on low-frequency foregrounds (section 2.2), the baseline PIXIE mission constrains electron pressure $\sigma(y) = 1.6 \times 10^{-8}$ and the electron temperature $\sigma(kT_e) = 0.17\,\mathrm{keV}$, providing a new window on structure formation.

Figure 10 compares the PIXIE constraints to the range of assumptions employed in simulations. We adopt the baseline PIXIE mission noise curves (appendix C) with a total of 7.6 months integration time on the cleanest 70% of the sky. In addition to the y-distortion and its relativistic correction, the Fisher forecast includes six astrophysical foregrounds with 11 free parameters as described in section 2.2. Additionally, 10% priors are assumed for both the

JCAP04(2025)020

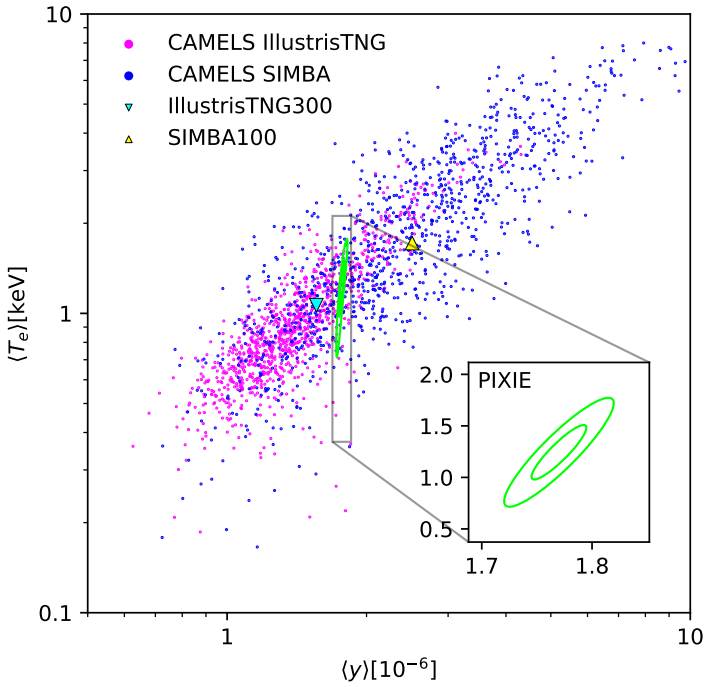

Figure 10. PIXIE constraints on the mean electron temperature and pressure in the post-recombination universe compared to the current range used in cosmological simulations.

synchrotron and free-free emission, and no curvature parameter for the synchrotron emission is included in this setup. The resulting limits differ from [37] in that both an updated noise curve and a different baseline integration time have been used.

Measurements of monopole y quantify the amount of feedback energy injected into the ionized gas, central to refining simulations. As can be seen in figure 10, current models of astrophysical feedback depend on highly uncertain parameters, yielding a wide range of predictions in the $y - T_e$ plane. More precise simulations reduce uncertainty in cosmological parameter estimates from large-scale structure. Cosmological probes dependent on baryonic feedback include weak gravitational lensing and the observable-mass relation of galaxy clusters. Questions such as concordance between the amplitude of fluctuations in the early and late universe, as well as the neutrino mass sum, are hindered by baryonic feedback uncertainty. Measurements of tSZ also constrain primordial non-Gaussianity [93] with complementarity to other probes, but at lower sensitivity. For a fuller discussion, see [94].

3.5 Star formation history

Traditional spectroscopic galaxy surveys have been used to measure both the star-formation-rate density (SFRD) and the metallicity. However, these surveys for line emission in individual galaxies have been limited by selection effects and small survey areas (sample variance), hampering comparison with galaxy evolution models [95]. In addition, measurements of the SFRD typically rely on optical data, which require corrections for dust extinction [96].

PIXIE will produce an unbiased measurement of the star formation history using line intensity mapping (LIM). LIM efficiently surveys the integral emission over a wide area,

JCAP04(2025)020

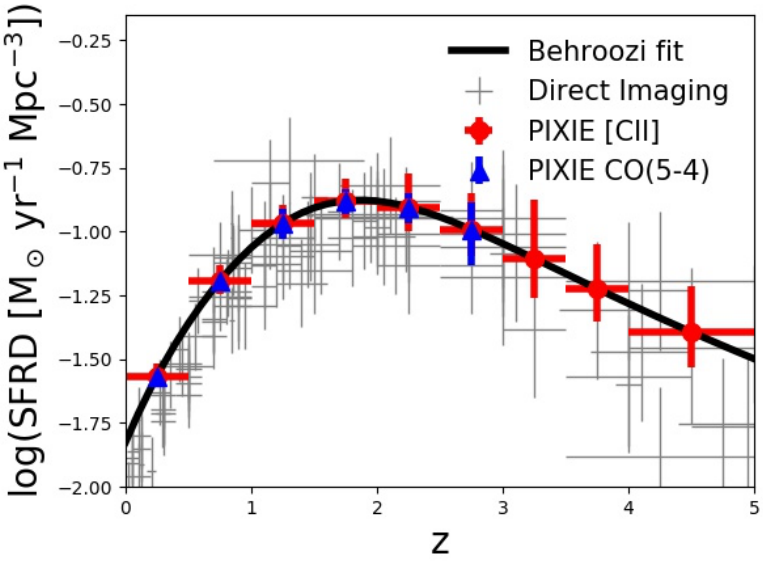

Figure 11. PIXIE constraints on the average star formation rate density from line intensity mapping of redshifted CO 5-4 and [CII] lines, compared to current measurements. PIXIE provides a legacy census of star formation across cosmic time, unaffected by sample variance or selection effects.

circumventing sample variance and selection effects. PIXIE surveys a large area, so it is not impacted by field-to-field scatter effects. This is especially valuable at $z < 0.5$ where direct detection surveys on small areas have high field scatter effects. LIM with PIXIE observes the integral of all gas, avoiding issues relating simulations to the complex selection [95].

Figure 11 shows SFRD recovered from simulations using the baseline PIXIE sensitivity. for the fiducial SFRD model [96]. PIXIE will measure both [CII] and CO emission. We assume the [CII] luminosity model from [97]

$$L_{\rm CII}(M,z) = \left(\frac{M}{M_1}\right)^{\beta} \exp(-N_1/M) \left(\frac{(1+z)^{2.7}}{1+[(1+z)/2.9)]^{5.6}}\right)^{\alpha} \tag{3.1}$$

such that the [CII] luminosity is related to the SFR by a power law, $L \propto {\rm SFR}^{\alpha}$. The parameters β, N_1, and M_1 are set at all redshifts using priors from [97]. We set α at each redshift in a different manner. We use the Santa Cruz semi-analytic model (SAM) [95, 98, 99], which predicts both [CII] luminosities and SFRs for galaxies, to fit α at each redshift using [CII] intensities and SFRDs from the SAM. For the SFRD forecast from PIXIE's CO(5-4) intensity measurement, we assume the Yang et al. (2019) CO(5-4) luminosity model, which is a fit to the Santa Cruz SAM. In this case we assume a linear relationship between the CO(5-4) luminosity and the SFR, such that the CO(5-4) intensity is proportional to the SFRD.

PIXIE will focus on CO, [CII] and [NII] emission, which originate from dense regions of the ISM and so are good tracers of both star formation [100, 101] and metallicity [102]. PIXIE's numerous narrow channels facilitate clean measurement across redshift [103], while the broad frequency coverage enables both [CII] and CO measurements at identical redshifts to provide independent tests of the CO vs [CII] luminosity-star formation rate relations.

JCAP04(2025)020

3.6 Cosmic infrared background

The Cosmic Infrared Background (CIB) is the integrated thermal emission of optical and ultraviolet light emitted by stars and active galactic nuclei, then absorbed and re-radiated by dust. It measures the energy release from the post-recombination universe and constrains the star formation history across cosmic time. Although the CIB amplitude is broadly consistent with known source populations, the comparison to integrated source counts is limited in part by the ∼6% uncertainty in the CIB amplitude [104–106]. PIXIE's absolute calibration determines the sky brightness to 0.1% accuracy at frequencies above 600 GHz [38]. Confusion with thermal emission from the diffuse Galactic cirrus and zodiacal emission will limit determination of the CIB monopole amplitude to comparable precision, providing a target for comparison with source counts.

PIXIE will also map the CIB distribution across the sky. The dipole anisotropy in the cosmic microwave background is usually attributed to the motion of the Solar System with respect to the rest frame of the surface of last scattering at redshift $z \sim 1100$. The observed homogeneity of the universe on scales larger than ∼100 Mpc implies that the integrated far-IR emission from galaxies at $z < 6$ should show a comparable kinematic dipole, with amplitude $\Delta I/I = 1.2 \times 10^{-3}$ in the same direction $(l, b) = (264.021°, 48.253°)$ as the CMB dipole [107]. Since the CIB represents the integrated emission from all galaxies, its dipole does not suffer from potential bias from survey completeness. A statistically significant difference in either amplitude or direction between the CMB and CIB dipoles would provide evidence for a non-kinematic component for the CMB dipole resulting from pre-inflationary physics [108, 109].

To quantify the PIXIE sensitivity to the CIB dipole, we generate a sky model with the nominal CMB, CIB, and Galactic foregrounds, including the dominant foregrounds from Galactic dust and zodiacal emission. We then add simulated instrument noise and perform a pixel-by-pixel fit of the CIB amplitude, CMB amplitude, and foreground amplitudes/spectral parameters (section 2.2) for 5000 realizations of the noise. We assume that the CIB spectral energy distribution is independent of direction on the sky, fitting a global CIB spectrum with amplitude fitted individually in each pixel. Foreground parameters (amplitude, temperatures, spectral indices) are fit on a pixel-by-pixel basis. The resulting distribution for the CIB in each pixel recovers the CIB dipole amplitude to 5% and direction to 4° uncertainty, where the uncertainties are dominated by confusion with the Galactic and zodiacal foregrounds.

3.7 Interstellar medium

Interstellar dust plays critical roles in the chemical evolution of galaxies [110, 111], the processing of optical and ultraviolet light [112–114] into the infrared [115–119], the thermodynamics of interstellar gas [120, 121], and the formation of stars and planets [122]. It is a primary reservoir of interstellar metals, but its composition and evolution throughout the galaxy are uncertain. The first full-sky measurements of the polarized dust spectrum from Planck and the unexpectedly-high fractional polarization of the dust emission defied predictions from pre-Planck dust models (e.g., [123]). These models posit that grains exist as two distinct populations of silicate or carbonaceous grains, and thus that either ISM processing is too slow to mix them or injection timescales are short enough to maintain pristine stardust populations

JCAP04(2025)020

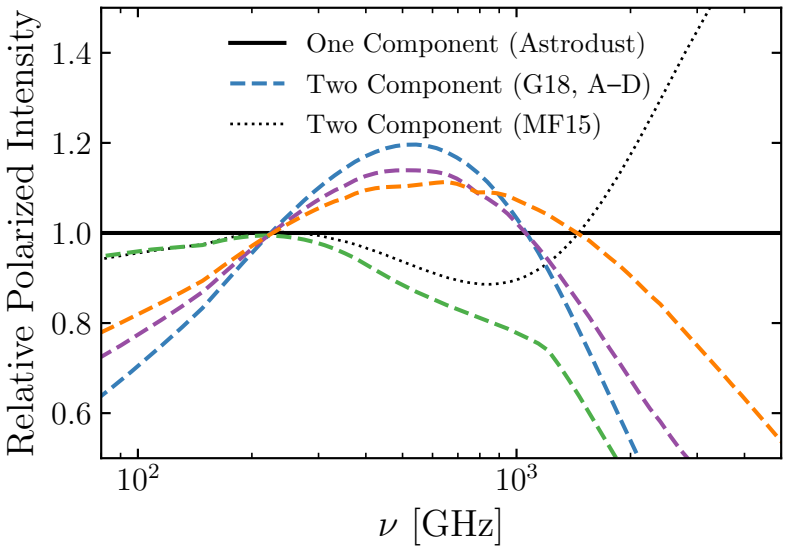

Figure 12. Predicted dust polarization spectra (normalized to the astrodust model) compared to the PIXIE sensitivity for a single representative high-latitude line of sight. PIXIE distinguishes between currently-viable models at high statistical confidence.

of distinct composition. If so, the dust spectrum in total intensity should differ from that in polarized intensity [124]. This is not observed at the microwave frequencies accessible to Planck [60] or the still higher frequencies observed by the BLASTPol balloon [125, 126]. Multi-component dust models have now been devised to respect Planck constraints [127, 128], while an alternative one-component model ("astrodust") has also been proposed [124, 129].

PIXIE's frequency coverage extending to the THz regime differentiates these dust modeling paradigms. Figure 12 compares models of polarized dust emission compatible with Planck data to the PIXIE baseline mission sensitivity. PIXIE data at THz frequencies discriminate between the current array of models at tens of standard deviations within each high-latitude line of sight.

Dust absorbs as well as emits. While correction for dust extinction is typically performed at optical and UV wavelengths, the low dust optical depth at much longer wavelengths has made such corrections negligible compared to instrument sensitivities. Figure 13 shows the effect of dust absorption of the CMB monopole, sometimes called "CMB shadow" [130, 131]. The absorption signal is comparable in amplitude to the predicted y and μ spectral distortions. PIXIE has the sensitivity to make the first detection of the cosmic microwave background absorption by dust grains, constraining the quantum behavior of dust grains [132–134].

PIXIE will also map line emission from Galactic molecular, atomic, and ionic species. Although the moderate spectral resolution prevents velocity-resolved measurements in the Galactic plane, PIXIE will map the velocity-integrated line emission over the full sky. We use low-SNR maps of the CO lines from Planck and the singly-ionized carbon and nitrogen lines from FIRAS to estimate the PIXIE line sensitivity at latitudes $|b| > 20°$. Table 4 lists the median per-pixel signal to noise ratio for these lines.

JCAP04(2025)020

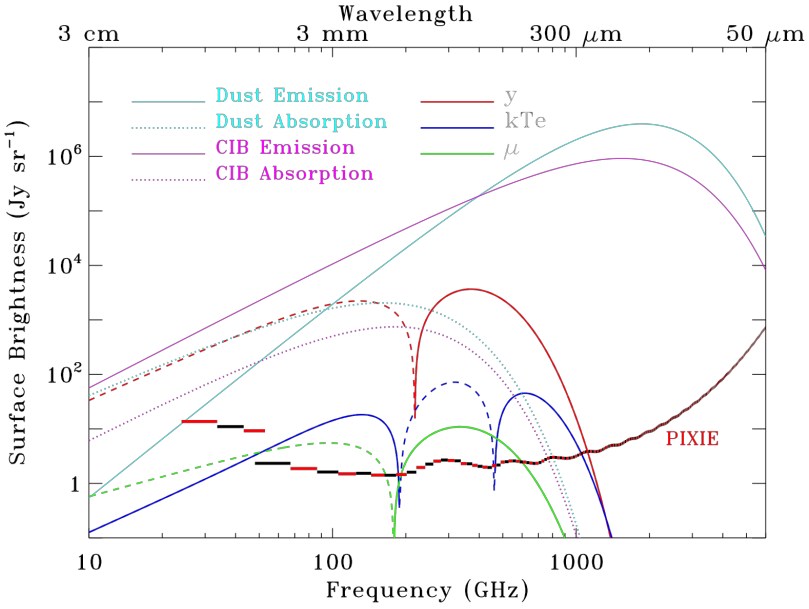

Figure 13. Solid lines show the amplitude of emission from the ISM (cyan) and CIB (magenta), while dotted lines show the absorption of the CMB monopole by these components. Absorption of the CMB monopole by dust or the CIB is comparable in amplitude to the cosmological signals and could be detected by PIXIE.

4 Discussion

PIXIE uses a single cryogenic Fourier transform spectrometer to measure the Stokes I, Q, U parameters at sensitivity $\sim$200 Jy sr^{-1} in each 2.65° diameter beam over the full sky, at frequencies from 28 GHz to 6 THz. The baseline 2-year mission spends equal time measuring spectral distortions (with an external blackbody calibrator deployed to block one beam) versus polarization (with the calibrator stowed so both beams view the sky). The resulting 7.6 months of integration in each mode over the cleanest 70% of the sky provides a robust detection of the spectral distortions from the mean electron pressure and temperature of the universe, and provides 95% confidence limits to B-mode polarization to detect the signal predicted from most single-field inflationary models. The fraction of time spent in each observing mode can be changed at any point throughout the mission. PIXIE carries no expendable cryogens; a longer mission dedicated to polarization would improve the polarization limits to $r < 0.9 \times 10^{-3}$ to test multi-field inflation models. Conversely, a longer mission dedicated primarily to spectral distortions would lower the current 95% confidence upper limit on the chemical potential to $|\mu| < 10^{-7}$. The resulting factor of 1000 improvement over the COBE/FIRAS limits opens an enormous discovery space for processes including dark matter, primordial black holes, and inflation. Appendix B summarizes instrumental improvements compared to FIRAS.

Foreground subtraction degrades the sensitivity to the chemical potential μ by a factor of 6–10 compared to the ideal case with no foregrounds. Improved foreground component separation requires additional channels at lower frequencies, without sacrificing sensitivity at higher frequencies. This cannot be accomplished with a single FTS: lengthening the optical phase delay to reduce the channel width (thereby squeezing in additional low-frequency

JCAP04(2025)020

Line	Median SNR[a]
CO J=1–0	0.1
CO J=2–1	2.2
CO J=3–2	10
CO J=4–3	26
CO J=5–4	27
CO J=6–5	26
CO J=7–6	11
C+ 158 um	5040
N+ 205 um	450

[a]Median per-pixel signal to noise ratio at $|b| > 30°$

Table 4. Line emission signal to noise ratio.

FTS Module	Channel Width	Lowest Frequency	Highest Frequency
Low-Freq	5 GHz	15 GHz	150 GHz
Mid-Freq	30 GHz	90 GHz	600 GHz
High-Freq	30 GHz	450 GHz	6 THz

Table 5. Potential Super-PIXIE configuration.

channels) degrades the sensitivity to continuum signals (section 2.1). As a compromise, PIXIE spends 30% of the integration time in a long-stroke mode to obtain low-frequency coverage, with the remaining 70% spent in short-stroke mode to maximize continuum sensitivity.

The choice of a single FTS is dictated by the $300 million (2022 USD) mission budget for NASA's MIDEX program.[2] A larger budget would allow a more ambitious instrument architecture. This could be accomplished within NASA's $1B Astrophysics Probe line[3] or ESA's L-class mission. Such a "Super-PIXIE" would employ 3 (or more) cryogenic FTS modules, each using the basic PIXIE design, but with channel width and optical passband (hence photon NEP) tuned to optimize the combined sensitivity to selected CMB signals. Table 5 shows one possible configuration. A low-frequency module would employ 5 GHz channel width over a passband 15–150 GHz to characterize the low-frequency foregrounds while avoiding photon noise from the CMB monopole at higher frequencies. A mid-frequency module would use wider 30 GHz channels over a passband 90–600 GHz to cover the cosmological signals. A high-frequency module would use 30 GHz channel width over the passband 450–6000 GHz to characterize the high-frequency foregrounds, setting the lowest frequency at 450 GHz to minimize the photon noise contribution from the CMB monopole. The two lower-frequency modules would image the sky in 7 sky pixels to increase the system etendue. Figure 14 compares the resulting sensitivity to both PIXIE and FIRAS. Such a Super-PIXIE mission could provide a 3σ detection of the minimal chemical potential distortion from dissipation of primordial density perturbations within the ΛCDM model.

[2]https://explorers.larc.nasa.gov/2021APMIDEX/MIDEX/index.html.
[3]https://explorers.larc.nasa.gov/2023APPROBE/announcements.html.

JCAP04(2025)020

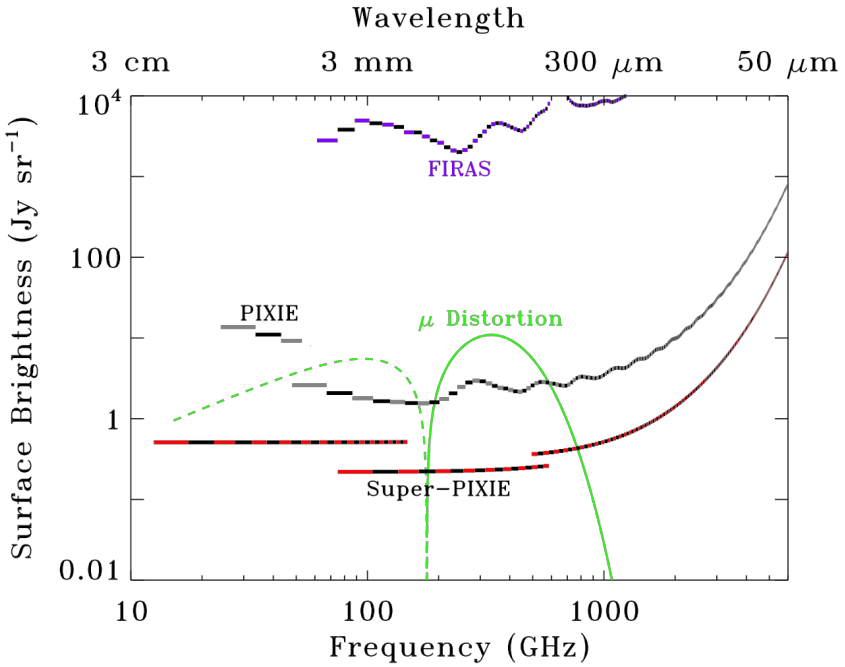

Figure 14. A Super-PIXIE mission with 3 FTS modules would tune the channel width and optical passband of each module to optimize the combined sensitivity to foregrounds and CMB spectral distortions.

Acknowledgments

This research was carried out in part at the Jet Propulsion Laboratory, California Institute of Technology, under a contract with the National Aeronautics and Space Administration. The cost information contained in this document is of a budgetary and planning nature and is intended for informational purposes only. It does not constitute a commitment on the part of JPL and/or Caltech.

A Data sampling and apodization

PIXIE uses physically large, multi-moded detectors to operate at background-limited sensitivity across a broad spectral range. Figure 15 shows the detector design. The detector absorbing element consists of 3 μm wide wires of micromachined crystalline silicon 12.7 mm long and spaced 30 μm apart. The absorber wires are degenerately doped with phosphorus to be metallic at all temperatures and absorb a single linear polarization. Un-doped cross-members every 300 μm maintain alignment; the structure is 85% open to minimize the cross section for cosmic ray impacts. A tensile Al_2O_3 film deposited on the wires outside of the active absorbing area maintains grid planarity within ±5 μm and raises the absorber resonant frequency above 1 kHz. Silicon legs suspend the bolometer and provide thermal isolation from a silicon frame heat sunk at 100 mK. Gold bars 0.5 μm thick at the end of the absorbing structure dominate the heat capacity to stabilize the thermal response [40]. Ion-implanted silicon thermistors measure the temperature fluctuations of the absorbing structure in response to optical power. Two identical arrays are hybridized back-to-back to give dual-polarization sensitivity within

JCAP04(2025)020

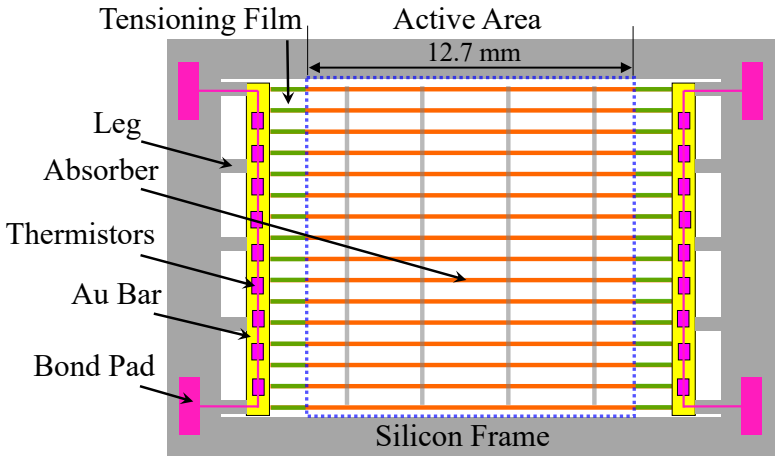

Figure 15. Schematic showing major elements of the PIXIE detectors. Doped silicon wires absorb a single linear polarization over etendue $4\,\mathrm{cm}^2\,\mathrm{sr}$.

each optical concentrator. Tensioned leads connect each bolometer to a cryogenic JFET amplifier, mitigating capacitive microphonic contamination of the signal band [135, 136]. The amplifier is AC biased above the $1/f$ knee of the JFET.

A double-sided interferogram with N_s samples over optical phase delay $[-L, L]$ returns spectra in $N_s/2$ channels at center frequencies $[0, 1, 2, \ldots, N_s/2] \times \Delta\nu$ where $\Delta\nu = c/(2L)$ is the synthesized channel width. The maximum mirror throw determines the channel width, while the number of samples determines the number of channels and hence the highest synthesized frequency. The MTM mirror hardware moves at constant phase velocity $v = 4\,\mathrm{mm\,s^{-1}}$ over maximum optical phase delay $\pm 16\,\mathrm{mm}$. The $512\,\mathrm{Hz}$ detector data rate thus provides 2048 samples for a single end-to-end mirror stroke over the maximum optical range, corresponding to 1024 synthesized channels with channel width $\Delta\nu = 9.6\,\mathrm{GHz}$ to maximum frequency $9.8\,\mathrm{THz}$. Software commands allow shorter mirror strokes and thus wider synthesized channels. The constant mirror velocity produces a fixed relation between the audio frequencies of the sampled data and the corresponding optical frequencies,

$$\nu_{\mathrm{data}} = \frac{v}{c}\nu_{\mathrm{opt}} \ . \tag{A.1}$$

Scattering filters limit the optical passband to frequencies below $6\,\mathrm{THz}$, corresponding to audio frequencies below $80\,\mathrm{Hz}$; synthesized channels at higher optical frequency contain noise but no optical signal.

PIXIE acquires data with the mirror moving in both directions. To minimize aliasing in the synthesized frequency spectra, the phase-delay mirror position must be controlled to $0.4\,\mu\mathrm{m}$ precision near the white-light null at zero optical phase delay. Figure 16 compares the PIXIE requirement to the performance of an engineering prototype. The mirrors are mounted on a double flexure suspension with a voice coil drive motor. A non-contacting capacitive position sensor provides position feedback within an active control loop. Passive electromagnetic dampers on both the mirror drive and flexures provide additional control stability. The measured position jitter exceeds requirements over the entire optical range.

JCAP04(2025)020

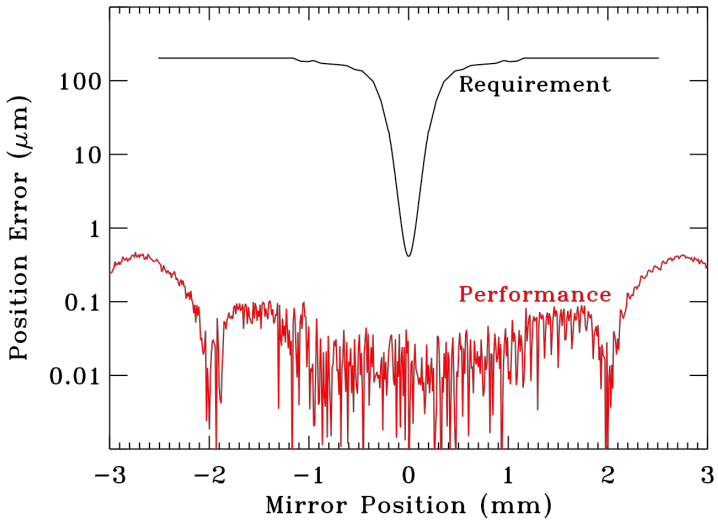

Figure 16. The measured position jitter for an engineering prototype phase delay mechanism exceeds the PIXIE requirements over the entire optical range.

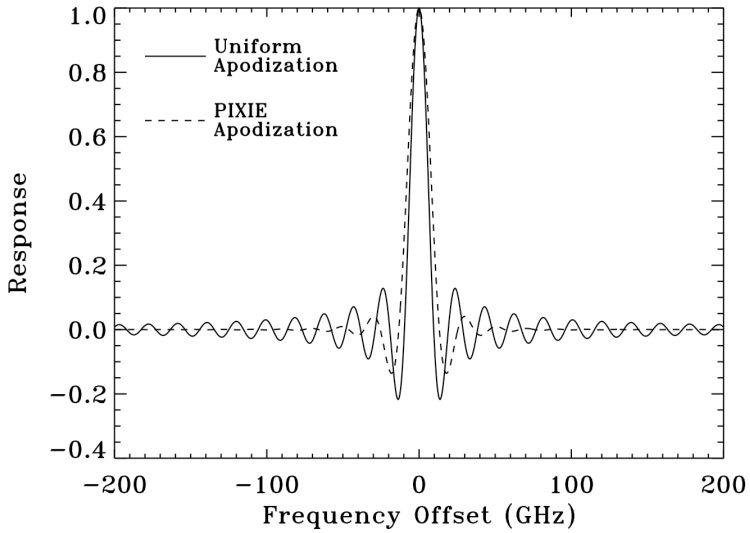

Figure 17. Frequency response after Fourier transform for different apodization of the sampled interferograms. The PIXIE apodization has broader channel width but much less ringing than uniform apodization.

Apodization of the Fourier transform determines the channel-to-channel covariance. For a given mirror throw, uniform weighting of the interferogram produces the narrowest channel width; however, the resulting spectra have channel-to-channel coupling described by a sinc function across a broad spectral range. PIXIE will use the apodization function

$$W(x) = (1 - x^4)^2 \tag{A.2}$$

where $x = z/z_{\rm max}$ is the fractional phase delay. Figure 17 compares the frequency response for each choice of apodization. The PIXIE apodization increases the channel width by 37%

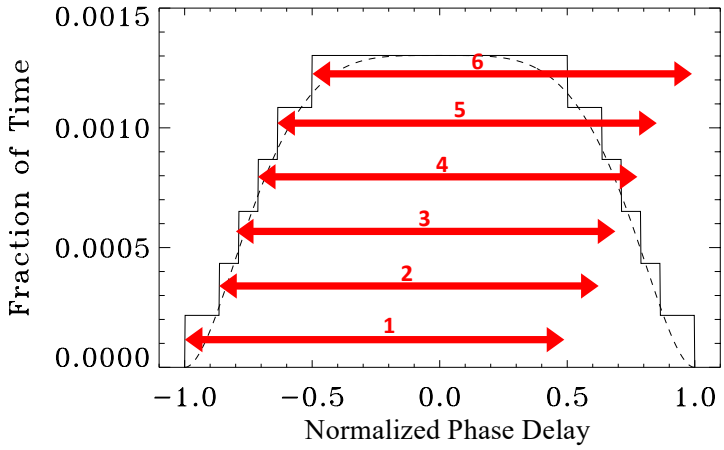

Figure 18. PIXIE varies the MTM stroke to apodize the observed interferograms. Each stroke uses 3 seconds to cover 3/4 of the total optical phase delay. A set of 6 different start/stop points (red bars) provides an integration time at each optical phase delay (solid line) closely approximating the desired apodization (dashed line).

compared to uniform apodization, but greatly reduces the ringing over larger frequency separations.

The apodization requires lower weight (fewer observations) for samples near the maximum optical phase delay. Continuously stroking the MTM over its full range every 4 seconds and then de-weighting samples (in the Fourier transform software) to achieve the desired apodization results in an effective loss of 29% of the available observing time. Instead, PIXIE uses a shorter MTM stroke covering 3/4 of the total range every 3 seconds, while periodically changing the start/stop points to build up the desired coverage versus optical phase delay. Figure 18 shows the concept. A set of 6 different strokes, each of the same length but starting at different positions, approximates the desired apodization to achieve 95% of the ideal observing efficiency.

B Comparison to FIRAS

The FIRAS spectrometer was a cryogenic Martin-Puplett interferometer whose two input ports compared signals from sky horn to emission from an internal blackbody reference. The sky horn could be blocked by a full-aperture blackbody to provide an absolute reference. Each of the two output ports used a dichroic splitter at 600 GHz to route the phase-delayed signal to a high-frequency or low-frequency detector [137]. PIXIE improves the sensitivity of the COBE/FIRAS measurements by a factor of more than 1000. We briefly review the principal design features leading to this improvement.

- **Detector temperature.** A liquid helium dewar cooled the FIRAS detectors to 1.5 K. At this temperature, the dominant noise source was phonon noise from the detectors, producing a system NEP of $4 \times 10^{-15}\,\mathrm{W}/\sqrt{\mathrm{Hz}}$. An adiabatic demagnetization refrigerator maintains the PIXIE detectors at 0.1 K to allow photon-limited NEP $2.7 \times 10^{-16}\,\mathrm{W}/\sqrt{\mathrm{Hz}}$ (section 2.1).

JCAP04(2025)020

Design Feature	Sensitivity Improvement
Detector Temperature	×17
Etendue	×3
Integration Time	×5
Interferogram Acquisition	×4
Total	×1020

Table 6. PIXIE vs FIRAS sensitivity improvements.

- **Etendue.** Although each of the 4 FIRAS detectors had etendue $A\Omega = 1.5\,\mathrm{cm}^2\,\mathrm{sr}^{-1}$, poor noise performance in two detectors meant that most of the sensitivity to CMB spectral distortions came from a single detector in the low-frequency dichroic channel at one of the two output ports. The larger PIXIE detectors each provide etendue $A\Omega = 4\,\mathrm{cm}^2\,\mathrm{sr}^{-1}$. PIXIE will fly four such detectors, each sensitive to the full optical passband.

- **Integration Time.** The FIRAS mission ended after 10 months when the liquid helium coolant ran out. Only 1 month of this time was spent observing the external blackbody calibrator, so that the sensitivity to sky spectra was limited by the signal-to-noise ratio of the calibration data. Since the single sky horn could not directly compare the sky to the external calibrator, the resulting comparison of separate sky/calibrator data sets incurred an additional $\sqrt{2}$ noise penalty. PIXIE has no expendable cryogens and can operate for extended periods. The baseline mission devotes 10.8 months to measurements of spectral distortions over the full sky, during which PIXIE's 2-beam design directly acquires the sky/calibrator difference spectrum.

- **Interferogram Acquisition.** FIRAS employed multiple scan modes to acquire the interferograms: a "short" stroke with 512 samples over a 1.2 cm path difference vs a "long" stroke with 2048 samples over a 5.9 cm path difference. Each stroke length was observed at 2 speeds: a "slow" stroke of 0.783 cm/s vs a "fast" stroke of 1.175 cm/s. The sensitivity for continuum sources such as the CMB was dominated by the short/slow combination, with little contribution from integration time devoted to other modes. PIXIE will divide its integration time between two different stroke lengths, with the bulk (70%) devoted to shorter strokes directed at the CMB continuum and the remainder used to obtain additional channels at frequencies below 60 GHz (section 2.1).

Table 6 summarizes the relative improvements in sensitivity.

Although FIRAS was not limited by systematic errors, the improved PIXIE sensitivity requires a corresponding reduction in potential sources of systematic error. Contributions to the PIXIE systematic error budget are discussed in [38, 39, 43]. We briefly review the principal design elements leading to a lower systematic error budget.

- **Isothermal Operation.** The bulk of the FIRAS instrument was cooled to 1.4 K by a superfluid liquid helium dewar, with the internal and external calibrators maintained near 2.725 K. The resulting 1.3 K gradient is a potential source for systematic error.

JCAP04(2025)020

PIXIE maintains all elements except the detectors within 5 mK of the CMB temperature, reducing the gradient source term by a factor of 265.

- **Blackbody Calibrator.** FIRAS compared the sky to an external trumpet-mute calibrator with emissivity $\epsilon > 0.99995$ (power reflection $R < -43\,\mathrm{dB}$) [138]. The PIXIE calibrator uses an array of absorbing cones with calculated reflectance $R < -65\,\mathrm{dB}$ [38].

- **Internal Reference.** FIRAS's two input ports compared the signal from the sky horn to an internal reference source with emissivity $\epsilon = 0.96$. FIRAS data required corrections both for reflections from the internal reference source as well as temperature gradients from heating at its tip [139]. PIXIE has no such source, and directly compares the sky to an external blackbody calibrator.

- **Cosmic Rays.** Cosmic ray hits to the FIRAS detectors were a dominant source of noise. FIRAS co-added multiple interferogram scans before downloading the data, preventing cleaning of cosmic ray hits in the time-ordered data. Despite the larger size of the PIXIE detectors, the PIXIE open construction has only 40% of the FIRAS effective area for particle hits. PIXIE downloads the full time-ordered data for individual interferograms, without onboard coaddition, allowing cosmic ray cleaning. After cleaning, cosmic rays produce an approximate white-noise spectrum a factor of 10 below the PIXIE photon noise [39].

- **Interferogram Acquisition.** FIRAS acquired double-sided interferograms so that the sky signal was entirely in the real part of the Fourier transform, but took data in only one mirror stroke direction. PIXIE will similarly acquire double-sided interferograms, but will take data in both directions to obtain additional time-reversal symmetries.

- **Instrument Symmetry.** The restricted volume within COBE's liquid helium dewar required FIRAS to use a folded optical path and a single sky horn. PIXIE is fully symmetric, with mirror-image beam-forming optics illuminating a fully-symmetric Martin-Puplett interferometer. The multiple symmetries enable jackknife tests to detect, model, and remove potential systematic errors [39].

C Mission noise curves

The tables below contain the center frequencies, sensitivity, and median noise level for a map pixel for the baseline 2-year PIXIE mission. The baseline 2-year mission assumes that 45% of observing time is spent with the calibrator deployed (sensitive to spectral distortions and polarization) and 45% with the calibrator stowed (sensitive to polarization only). Entries for polarization noise (table 8) include the polarization contribution from both modes. Noise levels assume 30% of the observing time in each mode is spent with narrow synthesized channel width (MTM long-stroke mode) and 70% with broad channel width (MTM short-stroke mode). See section 2.1 for details. The channel widths depend on the MTM mirror stroke and can be changed (within hardware limits) throughout the mission.

Data in these tables are also available on the Legacy Archive for Microwave Background Data (LAMBDA), https://lambda.gsfc.nasa.gov/product/pixie/pixie_baseline_noise_get.html.

JCAP04(2025)020

Center Frequency (GHz)	Sensitivity (Jy sr^{-1} $\sqrt{\text{sec}}$	Map Noise Jy sr^{-1}	Center Frequency (GHz)	Sensitivity (Jy sr^{-1} $\sqrt{\text{sec}}$	Map Noise Jy sr^{-1}
28.8	6.09E+04	2.53E+03	768.5	1.29E+04	5.37E+02
38.4	4.91E+04	2.04E+03	787.7	1.33E+04	5.53E+02
48.0	4.11E+04	1.71E+03	806.9	1.34E+04	5.59E+02
57.6	1.04E+04	4.33E+02	826.1	1.33E+04	5.55E+02
76.8	8.34E+03	3.47E+02	845.3	1.32E+04	5.47E+02
96.1	7.22E+03	3.00E+02	864.5	1.31E+04	5.46E+02
115.3	6.67E+03	2.78E+02	883.7	1.29E+04	5.39E+02
134.5	6.82E+03	2.84E+02	903.0	1.28E+04	5.34E+02
153.7	6.33E+03	2.63E+02	922.2	1.29E+04	5.35E+02
172.9	6.28E+03	2.61E+02	941.4	1.30E+04	5.41E+02
192.1	6.49E+03	2.70E+02	960.6	1.33E+04	5.51E+02
211.3	7.16E+03	2.98E+02	979.8	1.36E+04	5.66E+02
230.5	8.75E+03	3.64E+02	999.0	1.41E+04	5.86E+02
249.8	1.01E+04	4.19E+02	1018.2	1.46E+04	6.09E+02
269.0	1.14E+04	4.75E+02	1037.4	1.53E+04	6.36E+02
288.2	1.20E+04	4.98E+02	1056.7	1.59E+04	6.62E+02
307.4	1.17E+04	4.88E+02	1075.9	1.65E+04	6.85E+02
326.6	1.16E+04	4.82E+02	1095.1	1.69E+04	7.02E+02
345.8	1.03E+04	4.28E+02	1114.3	1.72E+04	7.14E+02
365.0	1.02E+04	4.25E+02	1133.5	1.73E+04	7.19E+02
384.2	9.56E+03	3.98E+02	1152.7	1.73E+04	7.18E+02
403.4	9.16E+03	3.81E+02	1171.9	1.72E+04	7.14E+02
422.7	8.84E+03	3.68E+02	1191.1	1.71E+04	7.11E+02
441.9	8.74E+03	3.64E+02	1210.3	1.71E+04	7.12E+02
461.1	9.42E+03	3.92E+02	1229.6	1.73E+04	7.18E+02
480.3	9.68E+03	4.03E+02	1248.8	1.76E+04	7.31E+02
499.5	1.10E+04	4.56E+02	1268.0	1.81E+04	7.52E+02
518.7	1.12E+04	4.64E+02	1287.2	1.87E+04	7.79E+02
537.9	1.15E+04	4.79E+02	1306.4	1.95E+04	8.09E+02
557.1	1.15E+04	4.80E+02	1325.6	2.02E+04	8.41E+02
576.4	1.13E+04	4.72E+02	1344.8	2.08E+04	8.65E+02
595.6	1.10E+04	4.59E+02	1364.0	2.14E+04	8.92E+02
614.8	1.10E+04	4.56E+02	1383.3	2.19E+04	9.13E+02
634.0	1.07E+04	4.46E+02	1402.5	2.22E+04	9.25E+02
653.2	1.05E+04	4.37E+02	1421.7	2.24E+04	9.31E+02
672.4	1.04E+04	4.31E+02	1440.9	2.24E+04	9.32E+02
691.6	1.04E+04	4.33E+02	1460.1	2.24E+04	9.33E+02
710.8	1.08E+04	4.48E+02	1479.3	2.25E+04	9.36E+02
730.1	1.15E+04	4.77E+02	1498.5	2.27E+04	9.46E+02
749.3	1.23E+04	5.10E+02	1517.7	2.31E+04	9.62E+02

Continued on next page

JCAP04(2025)020

Table 7 — continued from previous page

Center Frequency (GHz)	Sensitivity (Jy sr^{-1} $\sqrt{\text{sec}}$	Map Noise Jy sr^{-1}	Center Frequency (GHz)	Sensitivity (Jy sr^{-1} $\sqrt{\text{sec}}$	Map Noise Jy sr^{-1}
1536.9	2.37E+04	9.87E+02	2305.4	5.50E+04	2.29E+03
1556.2	2.45E+04	1.02E+03	2324.6	5.60E+04	2.33E+03
1575.4	2.54E+04	1.05E+03	2343.8	5.70E+04	2.37E+03
1594.6	2.61E+04	1.09E+03	2363.1	5.83E+04	2.42E+03
1613.8	2.71E+04	1.13E+03	2382.3	5.99E+04	2.49E+03
1633.0	2.79E+04	1.16E+03	2401.5	6.18E+04	2.57E+03
1652.2	2.87E+04	1.19E+03	2420.7	6.38E+04	2.66E+03
1671.4	2.92E+04	1.21E+03	2439.9	6.59E+04	2.74E+03
1690.6	2.95E+04	1.23E+03	2459.1	6.78E+04	2.82E+03
1709.9	2.97E+04	1.23E+03	2478.3	6.95E+04	2.89E+03
1729.1	2.98E+04	1.24E+03	2497.5	7.09E+04	2.95E+03
1748.3	3.00E+04	1.25E+03	2516.8	7.19E+04	2.99E+03
1767.5	3.03E+04	1.26E+03	2536.0	7.28E+04	3.03E+03
1786.7	3.08E+04	1.28E+03	2555.2	7.36E+04	3.06E+03
1805.9	3.15E+04	1.31E+03	2574.4	7.48E+04	3.11E+03
1825.1	3.24E+04	1.35E+03	2593.6	7.58E+04	3.15E+03
1844.3	3.33E+04	1.39E+03	2612.8	7.71E+04	3.21E+03
1863.6	3.45E+04	1.44E+03	2632.0	7.88E+04	3.28E+03
1882.8	3.57E+04	1.49E+03	2651.2	8.08E+04	3.36E+03
1902.0	3.69E+04	1.54E+03	2670.4	8.32E+04	3.46E+03
1921.2	3.79E+04	1.58E+03	2689.7	8.59E+04	3.57E+03
1940.4	3.87E+04	1.61E+03	2708.9	8.86E+04	3.69E+03
1959.6	3.93E+04	1.63E+03	2728.1	9.12E+04	3.79E+03
1978.8	3.97E+04	1.65E+03	2747.3	9.36E+04	3.89E+03
1998.0	4.00E+04	1.66E+03	2766.5	9.56E+04	3.98E+03
2017.2	4.03E+04	1.68E+03	2785.7	9.72E+04	4.04E+03
2036.5	4.07E+04	1.69E+03	2804.9	9.90E+04	4.12E+03
2055.7	4.14E+04	1.72E+03	2824.1	1.00E+05	4.17E+03
2074.9	4.22E+04	1.76E+03	2843.4	1.01E+05	4.22E+03
2094.1	4.33E+04	1.80E+03	2862.6	1.03E+05	4.28E+03
2113.3	4.46E+04	1.85E+03	2881.8	1.04E+05	4.35E+03
2132.5	4.61E+04	1.92E+03	2901.0	1.07E+05	4.43E+03
2151.7	4.76E+04	1.98E+03	2920.2	1.09E+05	4.54E+03
2170.9	4.92E+04	2.05E+03	2939.4	1.12E+05	4.67E+03
2190.2	5.06E+04	2.11E+03	2958.6	1.16E+05	4.81E+03
2209.4	5.18E+04	2.15E+03	2977.8	1.19E+05	4.96E+03
2228.6	5.27E+04	2.19E+03	2997.1	1.23E+05	5.11E+03
2247.8	5.33E+04	2.22E+03	3016.3	1.26E+05	5.25E+03
2267.0	5.39E+04	2.24E+03	3035.5	1.29E+05	5.37E+03
2286.2	5.44E+04	2.26E+03	3054.7	1.32E+05	5.48E+03

Continued on next page

JCAP04(2025)020

Table 7 — continued from previous page

Center Frequency (GHz)	Sensitivity (Jy sr^{-1} $\sqrt{\text{sec}}$	Map Noise Jy sr^{-1}	Center Frequency (GHz)	Sensitivity (Jy sr^{-1} $\sqrt{\text{sec}}$	Map Noise Jy sr^{-1}
3073.9	1.34E+05	5.57E+03	3842.4	3.17E+05	1.32E+04
3093.1	1.36E+05	5.65E+03	3861.6	3.24E+05	1.35E+04
3112.3	1.38E+05	5.72E+03	3880.8	3.31E+05	1.38E+04
3131.5	1.39E+05	5.80E+03	3900.0	3.37E+05	1.40E+04
3150.7	1.42E+05	5.89E+03	3919.2	3.42E+05	1.42E+04
3170.0	1.44E+05	6.01E+03	3938.4	3.47E+05	1.44E+04
3189.2	1.48E+05	6.15E+03	3957.6	3.52E+05	1.47E+04
3208.4	1.52E+05	6.31E+03	3976.9	3.59E+05	1.49E+04
3227.6	1.56E+05	6.50E+03	3996.1	3.66E+05	1.52E+04
3246.8	1.61E+05	6.69E+03	4015.3	3.74E+05	1.56E+04
3266.0	1.66E+05	6.89E+03	4034.5	3.83E+05	1.59E+04
3285.2	1.70E+05	7.08E+03	4053.7	3.93E+05	1.64E+04
3304.4	1.74E+05	7.24E+03	4072.9	4.04E+05	1.68E+04
3323.7	1.78E+05	7.40E+03	4092.1	4.16E+05	1.73E+04
3342.9	1.81E+05	7.54E+03	4111.3	4.27E+05	1.78E+04
3362.1	1.84E+05	7.65E+03	4130.6	4.37E+05	1.82E+04
3381.3	1.86E+05	7.76E+03	4149.8	4.47E+05	1.86E+04
3400.5	1.89E+05	7.87E+03	4169.0	4.55E+05	1.89E+04
3419.7	1.92E+05	7.99E+03	4188.2	4.62E+05	1.92E+04
3438.9	1.96E+05	8.14E+03	4207.4	4.70E+05	1.95E+04
3458.1	2.00E+05	8.32E+03	4226.6	4.77E+05	1.98E+04
3477.3	2.05E+05	8.53E+03	4245.8	4.85E+05	2.02E+04
3496.6	2.11E+05	8.77E+03	4265.0	4.94E+05	2.06E+04
3515.8	2.17E+05	9.03E+03	4284.2	5.05E+05	2.10E+04
3535.0	2.23E+05	9.26E+03	4303.5	5.16E+05	2.15E+04
3554.2	2.29E+05	9.53E+03	4322.7	5.30E+05	2.20E+04
3573.4	2.35E+05	9.77E+03	4341.9	5.44E+05	2.26E+04
3592.6	2.40E+05	1.00E+04	4361.1	5.60E+05	2.33E+04
3611.8	2.45E+05	1.02E+04	4380.3	5.75E+05	2.39E+04
3631.0	2.49E+05	1.04E+04	4399.5	5.89E+05	2.45E+04
3650.3	2.53E+05	1.05E+04	4418.7	6.02E+05	2.51E+04
3669.5	2.56E+05	1.07E+04	4437.9	6.14E+05	2.55E+04
3688.7	2.60E+05	1.08E+04	4457.2	6.24E+05	2.60E+04
3707.9	2.65E+05	1.10E+04	4476.4	6.34E+05	2.64E+04
3727.1	2.70E+05	1.13E+04	4495.6	6.44E+05	2.68E+04
3746.3	2.77E+05	1.15E+04	4514.8	6.56E+05	2.73E+04
3765.5	2.84E+05	1.18E+04	4534.0	6.67E+05	2.78E+04
3784.7	2.92E+05	1.21E+04	4553.2	6.80E+05	2.83E+04
3803.9	3.00E+05	1.25E+04	4572.4	6.96E+05	2.89E+04
3823.2	3.09E+05	1.28E+04	4591.6	7.13E+05	2.97E+04

Continued on next page

JCAP04(2025)020

Table 7 — continued from previous page

Center Frequency (GHz)	Sensitivity (Jy sr^{-1} $\sqrt{\text{sec}}$	Map Noise Jy sr^{-1}	Center Frequency (GHz)	Sensitivity (Jy sr^{-1} $\sqrt{\text{sec}}$	Map Noise Jy sr^{-1}
4610.8	7.32E+05	3.05E+04	5379.3	1.68E+06	7.00E+04
4630.1	7.52E+05	3.13E+04	5398.5	1.72E+06	7.15E+04
4649.3	7.72E+05	3.21E+04	5417.7	1.76E+06	7.32E+04
4668.5	7.92E+05	3.29E+04	5437.0	1.81E+06	7.51E+04
4687.7	8.10E+05	3.37E+04	5456.2	1.85E+06	7.70E+04
4706.9	8.26E+05	3.44E+04	5475.4	1.90E+06	7.90E+04
4726.1	8.41E+05	3.50E+04	5494.6	1.94E+06	8.08E+04
4745.3	8.55E+05	3.56E+04	5513.8	1.99E+06	8.26E+04
4764.5	8.70E+05	3.62E+04	5533.0	2.03E+06	8.43E+04
4783.8	8.84E+05	3.68E+04	5552.2	2.07E+06	8.59E+04
4803.0	8.99E+05	3.74E+04	5571.4	2.10E+06	8.73E+04
4822.2	9.16E+05	3.81E+04	5590.7	2.13E+06	8.87E+04
4841.4	9.36E+05	3.89E+04	5609.9	2.17E+06	9.01E+04
4860.6	9.58E+05	3.99E+04	5629.1	2.20E+06	9.17E+04
4879.8	9.83E+05	4.09E+04	5648.3	2.25E+06	9.34E+04
4899.0	1.01E+06	4.20E+04	5667.5	2.29E+06	9.54E+04
4918.2	1.04E+06	4.31E+04	5686.7	2.35E+06	9.76E+04
4937.4	1.06E+06	4.42E+04	5705.9	2.40E+06	1.00E+05
4956.7	1.09E+06	4.52E+04	5725.1	2.46E+06	1.03E+05
4975.9	1.11E+06	4.62E+04	5744.3	2.52E+06	1.05E+05
4995.1	1.13E+06	4.70E+04	5763.6	2.58E+06	1.07E+05
5014.3	1.15E+06	4.79E+04	5782.8	2.64E+06	1.10E+05
5033.5	1.17E+06	4.87E+04	5802.0	2.70E+06	1.12E+05
5052.7	1.19E+06	4.95E+04	5821.2	2.75E+06	1.14E+05
5071.9	1.21E+06	5.03E+04	5840.4	2.80E+06	1.16E+05
5091.1	1.23E+06	5.12E+04	5859.6	2.84E+06	1.18E+05
5110.4	1.26E+06	5.22E+04	5878.8	2.89E+06	1.20E+05
5129.6	1.28E+06	5.34E+04	5898.0	2.93E+06	1.22E+05
5148.8	1.32E+06	5.48E+04	5917.3	2.99E+06	1.24E+05
5168.0	1.35E+06	5.62E+04	5936.5	3.05E+06	1.27E+05
5187.2	1.39E+06	5.77E+04	5955.7	3.11E+06	1.30E+05
5206.4	1.42E+06	5.92E+04	5974.9	3.18E+06	1.32E+05
5225.6	1.46E+06	6.06E+04	5994.1	3.41E+06	1.42E+05
5244.8	1.49E+06	6.19E+04			
5264.1	1.52E+06	6.31E+04			
5283.3	1.54E+06	6.43E+04			
5302.5	1.57E+06	6.53E+04			
5321.7	1.59E+06	6.63E+04			
5340.9	1.62E+06	6.74E+04			
5360.1	1.65E+06	6.86E+04			

Table 7. Mission sensitivity to spectral distortions.

JCAP04(2025)020

Center Frequency (GHz)	Sensitivity (Jy sr^{-1} $\sqrt{\text{sec}}$	Map Noise Jy sr^{-1}	Center Frequency (GHz)	Sensitivity (Jy sr^{-1} $\sqrt{\text{sec}}$	Map Noise Jy sr^{-1}
28.8	8.61E+04	3.58E+03	1421.7	8.30E+03	3.45E+02
38.4	6.95E+04	2.89E+03	1460.1	8.32E+03	3.46E+02
48.0	5.82E+04	2.42E+03	1498.5	8.43E+03	3.51E+02
57.6	9.62E+03	4.00E+02	1536.9	8.79E+03	3.66E+02
76.8	7.93E+03	3.30E+02	1575.4	9.39E+03	3.91E+02
96.1	6.85E+03	2.85E+02	1613.8	1.00E+04	4.17E+02
115.3	2.57E+03	1.07E+02	1652.2	1.06E+04	4.42E+02
153.7	2.36E+03	9.81E+01	1690.6	1.09E+04	4.55E+02
192.1	2.41E+03	1.00E+02	1729.1	1.11E+04	4.60E+02
230.5	3.10E+03	1.29E+02	1767.5	1.12E+04	4.68E+02
269.0	4.20E+03	1.75E+02	1805.9	1.17E+04	4.86E+02
307.4	4.36E+03	1.81E+02	1844.3	1.24E+04	5.14E+02
345.8	3.85E+03	1.60E+02	1882.8	1.32E+04	5.51E+02
384.2	3.56E+03	1.48E+02	1921.2	1.41E+04	5.85E+02
422.7	3.29E+03	1.37E+02	1959.6	1.46E+04	6.06E+02
461.1	3.36E+03	1.40E+02	1998.0	1.48E+04	6.17E+02
499.5	3.89E+03	1.62E+02	2036.5	1.51E+04	6.29E+02
537.9	4.26E+03	1.77E+02	2074.9	1.57E+04	6.52E+02
576.4	4.21E+03	1.75E+02	2113.3	1.65E+04	6.87E+02
614.8	4.07E+03	1.69E+02	2151.7	1.76E+04	7.34E+02
653.2	3.90E+03	1.62E+02	2190.2	1.87E+04	7.80E+02
691.6	3.86E+03	1.61E+02	2228.6	1.95E+04	8.12E+02
730.1	4.24E+03	1.76E+02	2267.0	2.00E+04	8.31E+02
768.5	4.78E+03	1.99E+02	2305.4	2.04E+04	8.49E+02
806.9	4.98E+03	2.07E+02	2343.8	2.11E+04	8.79E+02
845.3	4.88E+03	2.03E+02	2382.3	2.22E+04	9.24E+02
883.7	4.81E+03	2.00E+02	2420.7	2.37E+04	9.84E+02
922.2	4.78E+03	1.99E+02	2459.1	2.51E+04	1.05E+03
960.6	4.91E+03	2.04E+02	2497.5	2.63E+04	1.09E+03
999.0	5.22E+03	2.17E+02	2536.0	2.70E+04	1.12E+03
1037.4	5.66E+03	2.35E+02	2574.4	2.77E+04	1.15E+03
1075.9	6.10E+03	2.54E+02	2612.8	2.86E+04	1.19E+03
1114.3	6.36E+03	2.64E+02	2651.2	3.00E+04	1.25E+03
1152.7	6.40E+03	2.66E+02	2689.7	3.18E+04	1.32E+03
1191.1	6.34E+03	2.64E+02	2728.1	3.38E+04	1.41E+03
1229.6	6.41E+03	2.66E+02	2766.5	3.54E+04	1.47E+03
1268.0	6.70E+03	2.79E+02	2804.9	3.67E+04	1.53E+03
1306.4	7.21E+03	3.00E+02	2843.4	3.76E+04	1.56E+03
1344.8	7.71E+03	3.21E+02	2881.8	3.87E+04	1.61E+03
1383.3	8.13E+03	3.38E+02	2920.2	4.05E+04	1.68E+03

Continued on next page

JCAP04(2025)020

Table 8 — continued from previous page

Center Frequency (GHz)	Sensitivity (Jy sr^{-1} $\sqrt{\text{sec}}$	Map Noise Jy sr^{-1}	Center Frequency (GHz)	Sensitivity (Jy sr^{-1} $\sqrt{\text{sec}}$	Map Noise Jy sr^{-1}
2958.6	4.29E+04	1.78E+03	4495.6	2.39E+05	9.93E+03
2997.1	4.55E+04	1.89E+03	4534.0	2.47E+05	1.03E+04
3035.5	4.78E+04	1.99E+03	4572.4	2.58E+05	1.07E+04
3073.9	4.96E+04	2.07E+03	4610.8	2.71E+05	1.13E+04
3112.3	5.10E+04	2.12E+03	4649.3	2.86E+05	1.19E+04
3150.7	5.25E+04	2.18E+03	4687.7	3.00E+05	1.25E+04
3189.2	5.48E+04	2.28E+03	4726.1	3.12E+05	1.30E+04
3227.6	5.79E+04	2.41E+03	4764.5	3.23E+05	1.34E+04
3266.0	6.14E+04	2.55E+03	4803.0	3.33E+05	1.39E+04
3304.4	6.45E+04	2.69E+03	4841.4	3.47E+05	1.44E+04
3342.9	6.72E+04	2.79E+03	4879.8	3.64E+05	1.52E+04
3381.3	6.92E+04	2.88E+03	4918.2	3.84E+05	1.60E+04
3419.7	7.12E+04	2.96E+03	4956.7	4.03E+05	1.68E+04
3458.1	7.41E+04	3.08E+03	4995.1	4.19E+05	1.74E+04
3496.6	7.81E+04	3.25E+03	5033.5	4.34E+05	1.81E+04
3535.0	8.25E+04	3.43E+03	5071.9	4.48E+05	1.86E+04
3573.4	8.71E+04	3.62E+03	5110.4	4.66E+05	1.94E+04
3611.8	9.08E+04	3.78E+03	5148.8	4.88E+05	2.03E+04
3650.3	9.37E+04	3.90E+03	5187.2	5.14E+05	2.14E+04
3688.7	9.65E+04	4.01E+03	5225.6	5.40E+05	2.25E+04
3727.1	1.00E+05	4.17E+03	5264.1	5.63E+05	2.34E+04
3765.5	1.05E+05	4.39E+03	5302.5	5.82E+05	2.42E+04
3803.9	1.11E+05	4.63E+03	5340.9	6.01E+05	2.50E+04
3842.4	1.17E+05	4.89E+03	5379.3	6.24E+05	2.59E+04
3880.8	1.23E+05	5.11E+03	5417.7	6.52E+05	2.71E+04
3919.2	1.27E+05	5.28E+03	5456.2	6.86E+05	2.86E+04
3957.6	1.31E+05	5.44E+03	5494.6	7.20E+05	2.99E+04
3996.1	1.36E+05	5.64E+03	5533.0	7.52E+05	3.13E+04
4034.5	1.42E+05	5.91E+03	5571.4	7.78E+05	3.24E+04
4072.9	1.50E+05	6.23E+03	5609.9	8.04E+05	3.34E+04
4111.3	1.58E+05	6.58E+03	5648.3	8.33E+05	3.46E+04
4149.8	1.66E+05	6.89E+03	5686.7	8.70E+05	3.62E+04
4188.2	1.71E+05	7.13E+03	5725.1	9.13E+05	3.80E+04
4226.6	1.77E+05	7.35E+03	5763.6	9.58E+05	3.98E+04
4265.0	1.83E+05	7.62E+03	5802.0	1.00E+06	4.16E+04
4303.5	1.91E+05	7.96E+03	5840.4	1.04E+06	4.31E+04
4341.9	2.02E+05	8.39E+03	5878.8	1.07E+06	4.45E+04
4380.3	2.13E+05	8.86E+03	5917.3	1.11E+06	4.61E+04
4418.7	2.23E+05	9.29E+03	5955.7	1.15E+06	4.80E+04
4457.2	2.31E+05	9.63E+03	5994.1	1.25E+06	5.22E+04

Table 8. Mission sensitivity to polarizations.

JCAP04(2025)020

References

[1] A.A. Penzias and R.W. Wilson, *A Measurement of excess antenna temperature at 4080-Mc/s*, *Astrophys. J.* **142** (1965) 419 [INSPIRE].

[2] T.F. HOWELL and J.R. SHAKESHAFT, *Spectrum of the 3° K Cosmic Microwave Radiation*, *Nature* **216** (1967) 753.

[3] G. De Amici, G.F. Smoot, S.D. Friedman and C. Witebsky, *New 33-GHz measurements of the cosmic background radiation intensity*, *Astrophys. J.* **298** (1985) 710 [INSPIRE].

[4] N. Mandolesi et al., *Measurements of the cosmic background radiation temperature at 6.3 centimeters*, *Astrophys. J.* **310** (1986) 561.

[5] A. Kogut et al., *The temperature of the cosmic microwave background radiation at a frequency of 10 GHz*, *Astrophys. J.* **325** (1988) 1.

[6] M. Bersanelli et al., *Measurements of the cosmic microwave background radiation temperature at 90 GHz*, *Astrophys. J.* **339** (1989) 632.

[7] M. Bersanelli et al., *Absolute measurement of the cosmic microwave background at 2 GHz*, *Astrophys. J.* **424** (1994) 517.

[8] G. de Amici et al., *The temperature of the cosmic microwave background radiation at 3.8 GHz — Results of a measurement from the South Pole site*, *Astrophys. J.* **381** (1991) 341.

[9] S. Levin et al., *A measurement of the cosmic microwave background temperature at 7.5 GHz*, *Astrophys. J.* **396** (1992) 3.

[10] M. Bensadoun et al., *Measurements of the cosmic microwave background temperature at 1.47 GHz*, *Astrophys. J.* **409** (1993) 1.

[11] M. Bersanelli et al., *Absolute measurement of the cosmic microwave background at 2 GHz*, *Astrophys. J.* **424** (1994) 517.

[12] S.T. Staggs, N.C. Jarosik, D.T. Wilkinson and E.J. Wollack, *An Absolute Measurement of the Cosmic Microwave Background Radiation Temperature at 20 Centimeters*, *Astrophys. J.* **458** (1996) 407.

[13] M. Gervasi et al., *TRIS II: search for CMB spectral distortions at 0.60, 0.82 and 2.5 GHz*, *Astrophys. J.* **688** (2008) 24 [arXiv:0807.4750] [INSPIRE].

[14] D.G. Johnson and D.T. Wilkinson, *A 1 percent measurement of the temperature of the cosmic microwave radiation at $\lambda = 1.2$ centimeters*, *Astrophys. J.* **313** (1987) L1.

[15] S.T. Staggs, N.C. Jarosik, S.S. Meyer and D.T. Wilkinson, *An Absolute measurement of the cosmic microwave background radiation temperature at 10.7-GHz*, *Astrophys. J. Lett.* **473** (1996) L1 [astro-ph/9609128] [INSPIRE].

[16] D.J. Fixsen et al., *ARCADE 2 Measurement of the Extra-Galactic Sky Temperature at 3–90 GHz*, *Astrophys. J.* **734** (2011) 5 [arXiv:0901.0555] [INSPIRE].

[17] D.M. Meyer and M. Jura, *A precise measurement of the cosmic microwave background temperature from optical observations of interstellar CN*, *Astrophys. J.* **297** (1985) 119.

[18] P. Crane, D.J. Hegyi, N. Mandolesi and A.C. Danks, *Cosmic background radiation temperature from CN absorption*, *Astrophys. J.* **309** (1986) 822.

[19] P. Crane, D.J. Hegyi, M.L. Kutner and N. Mandolesi, *Cosmic background radiation temperature at 2.64 millimeters*, *Astrophys. J.* **346** (1989) 136.

JCAP04(2025)020

[20] D.M. Meyer, K.C. Roth and I. Hawkins, *A precise CN measurement of the cosmic microwave background temperature at 1.32 millimeters*, *Astrophys. J.* **343** (1989) L1.

[21] M.E. Kaiser and E.L. Wright, *A precise measurement of the cosmic microwave background radiation temperature from CN observations toward Zeta Persei*, *Astrophys. J.* **356** (1990) L1.

[22] E. Palazzi et al., *A precise measurement of the cosmic background radiation at 1.32 millimeters*, *Astrophys. J.* **357** (1990) 14.

[23] K.C. Roth, D.M. Meyer and I. Hawkins, *Interstellar cyanogen and the temperature of the cosmic microwave background radiation*, *Astrophys. J.* **413** (1993) L67.

[24] A. Kogut et al., *Calibration and systematic error analysis for the COBE-DMR four-year sky maps*, *Astrophys. J.* **470** (1996) 653 [astro-ph/9601066] [INSPIRE].

[25] D.J. Fixsen et al., *The Cosmic Microwave Background spectrum from the full COBE FIRAS data set*, *Astrophys. J.* **473** (1996) 576 [astro-ph/9605054] [INSPIRE].

[26] H.P. Gush, M. Halpern and E.H. Wishnow, *Rocket measurement of the cosmic-background-radiation mm-wave spectrum*, *Phys. Rev. Lett.* **65** (1990) 537 [INSPIRE].

[27] D.J. Fixsen, *The Temperature of the Cosmic Microwave Background*, *Astrophys. J.* **707** (2009) 916 [arXiv:0911.1955] [INSPIRE].

[28] J.C. Mather et al., *Measurement of the Cosmic Microwave Background spectrum by the COBE FIRAS instrument*, *Astrophys. J.* **420** (1994) 439 [INSPIRE].

[29] WMAP collaboration, *Nine-Year Wilkinson Microwave Anisotropy Probe (WMAP) Observations: Cosmological Parameter Results*, *Astrophys. J. Suppl.* **208** (2013) 19 [arXiv:1212.5226] [INSPIRE].

[30] PLANCK collaboration, *Planck 2018 results. VI. Cosmological parameters*, *Astron. Astrophys.* **641** (2020) A6 [*Erratum ibid.* **652** (2021) C4] [arXiv:1807.06209] [INSPIRE].

[31] Y.B. Zeldovich and R.A. Sunyaev, *The Interaction of Matter and Radiation in a Hot-Model Universe*, *Astrophys. Space Sci.* **4** (1969) 301 [INSPIRE].

[32] R.A. Sunyaev and Y.B. Zeldovich, *Microwave background radiation as a probe of the contemporary structure and history of the universe*, *Ann. Rev. Astron. Astrophys.* **18** (1980) 537 [INSPIRE].

[33] L. Danese and G. de Zotti, *Double Compton process and the spectrum of the microwave background*, *Astron. Astrophys.* **107** (1982) 39.

[34] J.G. Bartlett and A. Stebbins, *Did the universe recombine?*, *Astrophys. J.* **371** (1991) 8.

[35] J. Chluba and R.A. Sunyaev, *The evolution of CMB spectral distortions in the early Universe*, *Mon. Not. Roy. Astron. Soc.* **419** (2012) 1294 [arXiv:1109.6552] [INSPIRE].

[36] J. Chluba et al., *New horizons in cosmology with spectral distortions of the cosmic microwave background*, *Exper. Astron.* **51** (2021) 1515 [arXiv:1909.01593] [INSPIRE].

[37] A. Kogut et al., *The Primordial Inflation Explorer (PIXIE): A Nulling Polarimeter for Cosmic Microwave Background Observations*, *JCAP* **07** (2011) 025 [arXiv:1105.2044] [INSPIRE].

[38] A. Kogut and D.J. Fixsen, *Calibration Method and Uncertainty for the Primordial Inflation Explorer (PIXIE)*, *JCAP* **05** (2020) 041 [arXiv:2002.00976] [INSPIRE].

[39] A. Kogut et al., *Systematic error mitigation for the PIXIE Fourier transform spectrometer*, *JCAP* **07** (2023) 057 [arXiv:2304.00091] [INSPIRE].

JCAP04(2025)020

[40] P.C. Nagler et al., *Multimode bolometer development for the PIXIE instrument*, *Proc. SPIE* **9914** (2016) 99141A [arXiv:1611.04466] [INSPIRE].

[41] A. Kogut, D.J. Fixsen and R.S. Hill, *Polarization properties of a broadband multi-moded concentrator*, *J. Opt. Soc. Am. A* **32** (2015) 1040 [arXiv:1503.04206].

[42] A. Kogut and D.J. Fixsen, *Polarized beam patterns from a multimoded feed for observations of the cosmic microwave background*, *J. Astron. Telesc. Instrum. Syst.* **4** (2018) 014006 [arXiv:1801.08971] [INSPIRE].

[43] P.C. Nagler, D.J. Fixsen, A. Kogut and G.S. Tucker, *Systematic effects in polarizing Fourier transform spectrometers for cosmic microwave background observations*, *Astrophys. J. Suppl.* **221** (2015) 21 [arXiv:1510.08089] [INSPIRE].

[44] P.J. Shirron et al., *Design of the PIXIE adiabatic demagnetization refrigerators*, *Cryogenics* **52** (2012) 140.

[45] E.J. Wollack et al., *Electromagnetic and Thermal Properties of a Conductively Loaded Epoxy*, *Int. J. Infrared MM Waves* **29** (2007) 51.

[46] D.T. Chuss et al., *A cryogenic thermal source for detector array characterization*, *Rev. Sci. Instrum.* **88** (2017) 104501 [arXiv:1707.05879].

[47] K.M. Górski et al., *HEALPix — A Framework for high resolution discretization, and fast analysis of data distributed on the sphere*, *Astrophys. J.* **622** (2005) 759 [astro-ph/0409513] [INSPIRE].

[48] J.C. Mather, *Bolometer noise: nonequilibrium theory*, *Appl. Opt.* **21** (1982) 1125.

[49] J. Zmuidzinas, *Thermal noise and correlations in photon detection*, *Appl. Opt.* **42** (2003) 4989.

[50] Z. Pan et al., *Compact millimeter-wavelength Fourier-transform spectrometer*, *Appl. Opt.* **58** (2019) 6257 [arXiv:1905.07399] [INSPIRE].

[51] M.H. Abitbol, J. Chluba, J.C. Hill and B.R. Johnson, *Prospects for Measuring Cosmic Microwave Background Spectral Distortions in the Presence of Foregrounds*, *Mon. Not. Roy. Astron. Soc.* **471** (2017) 1126 [arXiv:1705.01534] [INSPIRE].

[52] J.C. Hill et al., *Taking the Universe's Temperature with Spectral Distortions of the Cosmic Microwave Background*, *Phys. Rev. Lett.* **115** (2015) 261301 [arXiv:1507.01583] [INSPIRE].

[53] J. Chluba, *Which spectral distortions does ΛCDM actually predict?*, *Mon. Not. Roy. Astron. Soc.* **460** (2016) 227 [arXiv:1603.02496] [INSPIRE].

[54] J. Delabrouille et al., *A full sky, low foreground, high resolution CMB map from WMAP*, *Astron. Astrophys.* **493** (2009) 835 [arXiv:0807.0773] [INSPIRE].

[55] J. Delabrouille and J.-F. Cardoso, *Diffuse Source Separation in CMB Observations*, in *Data Analysis in Cosmology*, Springer, Berlin, Germany (2008), pg. 159 [DOI:10.1007/978-3-540-44767-2_6].

[56] S. Basak and J. Delabrouille, *A needlet ILC analysis of WMAP 7-year data: estimation of CMB temperature map and power spectrum*, *Mon. Not. Roy. Astron. Soc.* **419** (2012) 1163 [arXiv:1106.5383] [INSPIRE].

[57] PLANCK collaboration, *Planck 2018 results. IV. Diffuse component separation*, *Astron. Astrophys.* **641** (2020) A4 [arXiv:1807.06208] [INSPIRE].

[58] B. Thorne, J. Dunkley, D. Alonso and S. Naess, *The Python Sky Model: software for simulating the Galactic microwave sky*, *Mon. Not. Roy. Astron. Soc.* **469** (2017) 2821 [arXiv:1608.02841] [INSPIRE].

JCAP04(2025)020

[59] S. Hamimeche and A. Lewis, *Likelihood Analysis of CMB Temperature and Polarization Power Spectra*, *Phys. Rev. D* **77** (2008) 103013 [arXiv:0801.0554] [INSPIRE].

[60] PLANCK collaboration, *Planck 2018 results. XI. Polarized dust foregrounds*, *Astron. Astrophys.* **641** (2020) A11 [arXiv:1801.04945] [INSPIRE].

[61] G. Martínez-Solaeche, A. Karakci and J. Delabrouille, *A 3D model of polarized dust emission in the Milky Way*, *Mon. Not. Roy. Astron. Soc.* **476** (2018) 1310 [arXiv:1706.04162] [INSPIRE].

[62] V.A. Rubakov, M.V. Sazhin and A.V. Veryaskin, *Graviton Creation in the Inflationary Universe and the Grand Unification Scale*, *Phys. Lett. B* **115** (1982) 189 [INSPIRE].

[63] R. Fabbri and M. Pollock, *The Effect of Primordially Produced Gravitons upon the Anisotropy of the Cosmological Microwave Background Radiation*, *Phys. Lett. B* **125** (1983) 445 [INSPIRE].

[64] L.F. Abbott and M.B. Wise, *Constraints on Generalized Inflationary Cosmologies*, *Nucl. Phys. B* **244** (1984) 541 [INSPIRE].

[65] A.G. Polnarev, *Polarization and anisotropy induced in the microwave background by cosmological gravitational waves*, *Astron. Zh.* **62** (1985) 1041.

[66] R.L. Davis et al., *Cosmic microwave background probes models of inflation*, *Phys. Rev. Lett.* **69** (1992) 1856 [*Erratum ibid.* **70** (1993) 1733] [astro-ph/9207001] [INSPIRE].

[67] L.P. Grishchuk, *Cosmological perturbations of Quantum mechanical origin and anisotropy of the microwave background*, *Phys. Rev. Lett.* **70** (1993) 2371 [gr-qc/9304001] [INSPIRE].

[68] M. Kamionkowski, A. Kosowsky and A. Stebbins, *Statistics of cosmic microwave background polarization*, *Phys. Rev. D* **55** (1997) 7368 [astro-ph/9611125] [INSPIRE].

[69] U. Seljak and M. Zaldarriaga, *Signature of gravity waves in polarization of the microwave background*, *Phys. Rev. Lett.* **78** (1997) 2054 [astro-ph/9609169] [INSPIRE].

[70] R.A. Daly, *Spectral distortions of the microwave background radiation resulting from the damping of pressure waves*, *Astrophys. J.* **371** (1991) 14 [INSPIRE].

[71] W. Hu, D. Scott and J. Silk, *Power spectrum constraints from spectral distortions in the cosmic microwave background*, *Astrophys. J. Lett.* **430** (1994) L5 [astro-ph/9402045] [INSPIRE].

[72] J. Chluba, R. Khatri and R.A. Sunyaev, *CMB at 2x2 order: The dissipation of primordial acoustic waves and the observable part of the associated energy release*, *Mon. Not. Roy. Astron. Soc.* **425** (2012) 1129 [arXiv:1202.0057] [INSPIRE].

[73] R.A. Sunyaev and R. Khatri, *Unavoidable CMB spectral features and blackbody photosphere of our Universe*, *Int. J. Mod. Phys. D* **22** (2013) 1330014 [arXiv:1302.6553] [INSPIRE].

[74] J. Chluba, A.L. Erickcek and I. Ben-Dayan, *Probing the inflaton: Small-scale power spectrum constraints from measurements of the CMB energy spectrum*, *Astrophys. J.* **758** (2012) 76 [arXiv:1203.2681] [INSPIRE].

[75] A. Baur et al., *Spectral distortions from promising single and multifield inflationary models*, *JCAP* **04** (2024) 090 [arXiv:2310.13071] [INSPIRE].

[76] B. Cyr et al., *Disentangling the primordial nature of stochastic gravitational wave backgrounds with CMB spectral distortions*, *Mon. Not. Roy. Astron. Soc.* **528** (2024) 883 [arXiv:2309.02366] [INSPIRE].

[77] LIGO SCIENTIFIC and VIRGO collaborations, *Observation of Gravitational Waves from a Binary Black Hole Merger*, *Phys. Rev. Lett.* **116** (2016) 061102 [arXiv:1602.03837] [INSPIRE].

JCAP04(2025)020

[78] NANOGrav collaboration, *The NANOGrav 15 yr Data Set: Evidence for a Gravitational-wave Background*, *Astrophys. J. Lett.* **951** (2023) L8 [arXiv:2306.16213] [INSPIRE].

[79] J. Antoniadis et al., *The International Pulsar Timing Array second data release: Search for an isotropic gravitational wave background*, *Mon. Not. Roy. Astron. Soc.* **510** (2022) 4873 [arXiv:2201.03980] [INSPIRE].

[80] D.J. Reardon et al., *Search for an Isotropic Gravitational-wave Background with the Parkes Pulsar Timing Array*, *Astrophys. J. Lett.* **951** (2023) L6 [arXiv:2306.16215] [INSPIRE].

[81] H. Xu et al., *Searching for the Nano-Hertz Stochastic Gravitational Wave Background with the Chinese Pulsar Timing Array Data Release I*, *Res. Astron. Astrophys.* **23** (2023) 075024 [arXiv:2306.16216] [INSPIRE].

[82] M. Tagliazucchi, M. Braglia, F. Finelli and M. Pieroni, *Quest for CMB spectral distortions to probe the scalar-induced gravitational wave background interpretation of pulsar timing array data*, *Phys. Rev. D* **111** (2025) L021305 [arXiv:2310.08527] [INSPIRE].

[83] E. Calabrese, D. Alonso and J. Dunkley, *Complementing the ground-based CMB-S4 experiment on large scales with the PIXIE satellite*, *Phys. Rev. D* **95** (2017) 063504 [arXiv:1611.10269] [INSPIRE].

[84] H. Tashiro, J. Silk and D.J.E. Marsh, *Constraints on primordial magnetic fields from CMB distortions in the axiverse*, *Phys. Rev. D* **88** (2013) 125024 [arXiv:1308.0314] [INSPIRE].

[85] D.J.E. Marsh, *Axion Cosmology*, *Phys. Rept.* **643** (2016) 1 [arXiv:1510.07633] [INSPIRE].

[86] B.J. Carr, K. Kohri, Y. Sendouda and J. Yokoyama, *New cosmological constraints on primordial black holes*, *Phys. Rev. D* **81** (2010) 104019 [arXiv:0912.5297] [INSPIRE].

[87] J.L. Feng, *Dark Matter Candidates from Particle Physics and Methods of Detection*, *Ann. Rev. Astron. Astrophys.* **48** (2010) 495 [arXiv:1003.0904] [INSPIRE].

[88] J.L. Aalberts et al., *Precision constraints on radiative neutrino decay with CMB spectral distortion*, *Phys. Rev. D* **98** (2018) 023001 [arXiv:1803.00588] [INSPIRE].

[89] P. McDonald, R.J. Scherrer and T.P. Walker, *Cosmic microwave background constraint on residual annihilations of relic particles*, *Phys. Rev. D* **63** (2001) 023001 [astro-ph/0008134] [INSPIRE].

[90] N. Battaglia et al., *Simulations of the Sunyaev-Zel'dovich Power Spectrum with AGN Feedback*, *Astrophys. J.* **725** (2010) 91 [arXiv:1003.4256] [INSPIRE].

[91] A.M.C.L. Brun, I.G. McCarthy, J. Schaye and T.J. Ponman, *Towards a realistic population of simulated galaxy groups and clusters*, *Mon. Not. Roy. Astron. Soc.* **441** (2014) 1270 [arXiv:1312.5462] [INSPIRE].

[92] L. Thiele et al., *Percent-level constraints on baryonic feedback with spectral distortion measurements*, *Phys. Rev. D* **105** (2022) 083505 [arXiv:2201.01663] [INSPIRE].

[93] J.C. Hill and E. Pajer, *Cosmology from the thermal Sunyaev-Zel'dovich power spectrum: Primordial non-Gaussianity and massive neutrinos*, *Phys. Rev. D* **88** (2013) 063526 [arXiv:1303.4726] [INSPIRE].

[94] L. Thiele et al., *Percent-level constraints on baryonic feedback with spectral distortion measurements*, *Phys. Rev. D* **105** (2022) 083505 [arXiv:2201.01663] [INSPIRE].

[95] G. Popping et al., *The art of modelling CO, [C I], and [C II] in cosmological galaxy formation models*, *Mon. Not. Roy. Astron. Soc.* **482** (2018) 4906 [arXiv:1805.11093].

JCAP04(2025)020

[96] P. Madau and M. Dickinson, *Cosmic Star Formation History*, *Ann. Rev. Astron. Astrophys.* **52** (2014) 415 [arXiv:1403.0007] [INSPIRE].

[97] H. Padmanabhan, *Constraining the evolution of [C II] intensity through the end stages of reionization*, *Mon. Not. Roy. Astron. Soc.* **488** (2019) 3014 [arXiv:1811.01968] [INSPIRE].

[98] R.S. Somerville, G. Popping and S.C. Trager, *Star formation in semi-analytic galaxy formation models with multiphase gas*, *Mon. Not. Roy. Astron. Soc.* **453** (2015) 4338 [arXiv:1503.00755].

[99] S. Yang et al., *An Empirical Representation of a Physical Model for the ISM [C II], CO, and [C I] Emission at Redshift* $1 \leq z \leq 9$, *Astrophys. J.* **929** (2022) [arXiv:2108.07716] [INSPIRE].

[100] F. Bigiel et al., *The Star Formation Law in Nearby Galaxies on Sub-Kpc Scales*, *Astron. J.* **136** (2008) 2846 [arXiv:0810.2541] [INSPIRE].

[101] F. Bigiel et al., *A Constant Molecular Gas Depletion Time in Nearby Disk Galaxies*, *Astrophys. J. Lett.* **730** (2011) L13 [arXiv:1102.1720] [INSPIRE].

[102] T. Nagao et al., *ALMA reveals a chemically evolved submillimeter galaxy at* $z = 4.76$, *Astron. Astrophys.* **542** (2012) L34 [arXiv:1205.4834] [INSPIRE].

[103] E.R. Switzer, *Tracing the cosmological evolution of stars and cold gas with CMB spectral surveys*, *Astrophys. J.* **838** (2017) 82 [arXiv:1703.07832] [INSPIRE].

[104] D.J. Fixsen et al., *The Spectrum of the extragalactic far infrared background from the COBE FIRAS observations*, *Astrophys. J.* **508** (1998) 123 [astro-ph/9803021] [INSPIRE].

[105] N. Odegard et al., *Determination of the Cosmic Infrared Background from COBE/FIRAS and Planck HFI Observations*, *Astrophys. J.* **877** (2019) 40 [arXiv:1904.11556] [INSPIRE].

[106] S. Duivenvoorden et al., *Have we seen all the galaxies that comprise the cosmic infrared background at* $250\,mum \leq \lambda \leq 500\,mum$*?*, *Mon. Not. Roy. Astron. Soc.* **491** (2020) 1355 [arXiv:1911.01437].

[107] PLANCK collaboration, *Planck 2018 results. I. Overview and the cosmological legacy of Planck*, *Astron. Astrophys.* **641** (2020) A1 [arXiv:1807.06205] [INSPIRE].

[108] A.R. King and G.F.R. Ellis, *Tilted homogeneous cosmological models*, *Commun. Math. Phys.* **31** (1973) 209 [INSPIRE].

[109] P. Tiwari, R. Kothari and P. Jain, *Superhorizon Perturbations: A Possible Explanation of the Hubble-Lemaître Tension and the Large-scale Anisotropy of the Universe*, *Astrophys. J. Lett.* **924** (2022) L36 [arXiv:2111.02685] [INSPIRE].

[110] E. Dwek, *Interstellar dust: What is it, how does it evolve, and what are its observational consequences?*, *AIP Conf. Proc.* **761** (2005) 103 [astro-ph/0412344] [INSPIRE].

[111] R.S. Asano, T.T. Takeuchi, H. Hirashita and A.K. Inoue, *Dust formation history of galaxies: a critical role of metallicity for the dust mass growth by accreting materials in the interstellar medium*, *Earth Planets Space* **65** (2013) 213 [arXiv:1206.0817] [INSPIRE].

[112] B.D. Savage and J.S. Mathis, *Observed properties of interstellar dust*, *Ann. Rev. Astron. Astrophys.* **17** (1979) 73 [INSPIRE].

[113] E.L. Fitzpatrick, *Correcting for the effects of interstellar extinction*, *Publ. Astron. Soc. Pac.* **111** (1999) 63 [astro-ph/9809387] [INSPIRE].

[114] J.A. Cardelli, G.C. Clayton and J.S. Mathis, *The relationship between infrared, optical, and ultraviolet extinction*, *Astrophys. J.* **345** (1989) 245 [INSPIRE].

JCAP04(2025)020

[115] W.T. Reach et al., *Far-infrared spectral observations of the galaxy by COBE*, *Astrophys. J.* **451** (1995) 188 [astro-ph/9504056] [INSPIRE].

[116] D.P. Finkbeiner, M. Davis and D.J. Schlegel, *Extrapolation of galactic dust emission at 100 microns to CMBR frequencies using FIRAS*, *Astrophys. J.* **524** (1999) 867 [astro-ph/9905128] [INSPIRE].

[117] WMAP collaboration, *First year Wilkinson Microwave Anisotropy Probe (WMAP) observations: Foreground emission*, *Astrophys. J. Suppl.* **148** (2003) 97 [astro-ph/0302208] [INSPIRE].

[118] PLANCK collaboration, *Planck 2013 results. XI. All-sky model of thermal dust emission*, *Astron. Astrophys.* **571** (2014) A11 [arXiv:1312.1300] [INSPIRE].

[119] PLANCK collaboration, *Planck 2015 results. X. Diffuse component separation: Foreground maps*, *Astron. Astrophys.* **594** (2016) A10 [arXiv:1502.01588] [INSPIRE].

[120] I. Millán-Irigoyen, M. Mollá and Y. Ascasibar, *Chemical evolution of galaxies: emerging dust and the different gas phases in a new multiphase code*, *Mon. Not. Roy. Astron. Soc.* **494** (2020) 146 [arXiv:1904.11215].

[121] A.G.G.M. Tielens, *Dust Formation in Astrophysical Environments: The Importance of Kinetics*, *Front. Astron. Space Sci.* **9** (2022) 908217 [arXiv:2206.01548].

[122] D. Wiebe, *Dust in Star Forming Regions — A Review*, in the proceedings of the *PoS* **269** (2017) 0023.

[123] B.T. Draine and A.A. Fraisse, *Polarized Far-Infrared and Submillimeter Emission from Interstellar Dust*, *Astrophys. J.* **696** (2009) 1 [*Erratum ibid.* **757** (2012) 106] [arXiv:0809.2094] [INSPIRE].

[124] B.T. Draine and B.S. Hensley, *The Dielectric Function of "Astrodust" and Predictions for Polarization in the* 3.4 *and* 10 μm *Features*, *Astrophys. J.* **909** (2021) 94 [arXiv:2009.11314].

[125] P.C. Ashton et al., *First Observation of the Submillimeter Polarization Spectrum in a Translucent Molecular Cloud*, *Astrophys. J.* **857** (2018) 10 [arXiv:1707.02936] [INSPIRE].

[126] J.A. Shariff et al., *Submillimeter Polarization Spectrum of the Carina Nebula*, *Astrophys. J.* **872** (2019) 197 [arXiv:1809.06375].

[127] V. Guillet et al., *Dust models compatible with Planck intensity and polarization data in translucent lines of sight*, *Astron. Astrophys.* **610** (2018) A16 [arXiv:1710.04598] [INSPIRE].

[128] N. Ysard et al., *THEMIS 2.0: A self-consistent model for dust extinction, emission, and polarisation*, *Astron. Astrophys.* **684** (2024) A34 [arXiv:2401.07739] [INSPIRE].

[129] B.S. Hensley and B.T. Draine, *The Astrodust+PAH Model: A Unified Description of the Extinction, Emission, and Polarization from Dust in the Diffuse Interstellar Medium*, *Astrophys. J.* **948** (2023) 55 [arXiv:2208.12365].

[130] M. Nashimoto, M. Hattori and Y. Chinone, *CMB Shadows: The Effect of Interstellar Extinction on Cosmic Microwave Background Polarization and Temperature Anisotropy*, *Astrophys. J. Lett.* **895** (2020) L21 [arXiv:2005.06614] [INSPIRE].

[131] I.A. Zelko and D.P. Finkbeiner, *Impact of Dust on Spectral Distortion Measurements of the Cosmic Microwave Background*, *Astrophys. J.* **914** (2021) 68 [arXiv:2010.06589] [INSPIRE].

[132] J.R. Bond, B.J. Carr and C.J. Hogan, *Cosmic backgrounds from primeval dust*, *Astrophys. J.* **367** (1991) 420 [INSPIRE].

JCAP04(2025)020

[133] E.L. Wright, *On the long-wavelength absorption by interstellar dust*, *Astrophys. J.* **375** (1991) 608.

[134] V. Vavrycuk, *Missing dust signature in the cosmic microwave background*, *Mon. Not. Roy. Astron. Soc.* **470** (2017) L44 [arXiv:1706.04771] [INSPIRE].

[135] R.L. Kelley et al., *The Suzaku High Resolution X-Ray Spectrometer*, *Publ. Astron. Soc. Jap.* **59** (2007) S77.

[136] F.S. Porter et al., *The detector subsystem for the SXS instrument on the ASTRO-H Observatory*, *Proc. SPIE* **7732** (2010) 77323J.

[137] J.C. Mather, D.J. Fixsen and R.A. Shafer, *Design for the COBE far-infrared absolute spectrophotometer*, in the proceedings of the *Infrared Spaceborne Remote Sensing*, *Proc. SPIE* **2019** (1993) 168.

[138] J.C. Mather et al., *Calibrator design for the COBE far infrared absolute spectrophotometer (FIRAS)*, *Astrophys. J.* **512** (1999) 511 [astro-ph/9810373] [INSPIRE].

[139] D.J. Fixsen et al., *Calibration of the Far Infrared Absolute Spectrophotometer (FIRAS) on the Cosmic Background Explorer (COBE)*, *Astrophys. J.* **420** (1994) 457 [INSPIRE].

JCAP04(2025)020